JGR Solid Earth

RESEARCH ARTICLE
10.1029/2018JB016736

Low-Temperature Plasticity in Olivine: Grain Size, Strain Hardening, and the Strength of the Lithosphere

Lars N. Hansen[1], Kathryn M. Kumamoto[2], Christopher A. Thom[3], David Wallis[4], William B. Durham[5], David L. Goldsby[3], Thomas Breithaupt[1], Cameron D. Meyers[6], and David L. Kohlstedt[6]

[1]Department of Earth Sciences, University of Oxford, Oxford, UK, [2]Department of Geological Sciences, Stanford University, Stanford, CA, USA, [3]Department of Earth and Environmental Science, University of Pennsylvania, Philadelphia, PA, USA, [4]Department of Earth Sciences, Utrecht University, Utrecht, The Netherlands, [5]Department of Earth, Atmospheric, and Planetary Sciences, Massachusetts Institute of Technology, Cambridge, MA, USA, [6]Department of Earth Sciences, University of Minnesota, Twin Cities, Minneapolis, MN, USA

Abstract Plastic deformation of olivine at relatively low temperatures (i.e., low-temperature plasticity) likely controls the strength of the lithospheric mantle in a variety of geodynamic contexts. Unfortunately, laboratory estimates of the strength of olivine deforming by low-temperature plasticity vary considerably from study to study, limiting confidence in extrapolation to geological conditions. Here we present the results of deformation experiments on olivine single crystals and aggregates conducted in a deformation-DIA at confining pressures of 5 to 9 GPa and temperatures of 298 to 1473 K. These results demonstrate that, under conditions in which low-temperature plasticity is the dominant deformation mechanism, fine-grained samples are stronger at yield than coarse-grained samples, and the yield stress decreases with increasing temperature. All samples exhibited significant strain hardening until an approximately constant flow stress was reached. The magnitude of the increase in stress from the yield stress to the flow stress was independent of grain size and temperature. Cyclical loading experiments revealed a Bauschinger effect, wherein the initial yield strength is higher than the yield strength during subsequent cycles. Both strain hardening and the Bauschinger effect are interpreted to result from the development of back stresses associated with long-range dislocation interactions. We calibrated a constitutive model based on these observations, and extrapolation of the model to geological conditions predicts that the strength of the lithosphere at yield is low compared to previous experimental predictions but increases significantly with increasing strain. Our results resolve apparent discrepancies in recent observational estimates of the strength of the oceanic lithosphere.

Key Points:
- D-DIA experiments were conducted on stacked samples of olivine, allowing precise determination of yield strength and subsequent hardening
- Olivine deforming in the low-temperature plasticity regime is stronger for smaller grain sizes and exhibits significant strain hardening
- We calibrate a model based on dislocation interactions that explains discrepancies among previous estimates of lithospheric strength

Correspondence to:
L. N. Hansen,
lars.hansen@earth.ox.ac.uk

Citation:
Hansen, L. N., Kumamoto, K. M., Thom, C. A., Wallis, D., Durham, W. B., Goldsby, D. L., et al. (2019). Low-temperature plasticity in olivine: Grain size, strain hardening, and the strength of the lithosphere. *Journal of Geophysical Research: Solid Earth*, *124*. https://doi.org/10.1029/2018JB016736

Received 18 SEP 2018
Accepted 20 MAR 2019
Accepted article online 25 MAR 2019

1. Introduction

The strength of Earth's lithosphere directly influences a wide variety of large-scale geodynamic processes. Correspondingly, considerable effort has been focused on characterizing the strength of the rocks that comprise the lithosphere through laboratory-based deformation experiments (e.g., Sibson, 1977; Brace & Kohlstedt, 1980; Kohlstedt et al., 1995). This research established models for the variation in general deformation mode as a function of depth into Earth's interior, suggesting that the integrated strength of the lithosphere depends intimately on the strength of ductile rocks in deeper and hotter regions. Mechanical data and microstructural observations commonly indicate that this ductile deformation is controlled by the motion of lattice dislocations. At the high temperatures characteristic of Earth's deep interior, dislocation motion is likely limited by diffusive processes, particularly those dislocations involved in dislocation climb (e.g., Karato et al., 1993; Kohlstedt & Hansen, 2015; Weertman, 1970). At the colder temperatures characteristic of the strongest portions of the lithosphere, however, diffusion is less active and deformation is limited by dislocation glide. Ductile deformation in this regime is often referred to as low-temperature plasticity (Frost & Ashby, 1982, p. 7). Thus, the maximum stress supported by the lithosphere depends strongly on deformation by low-temperature plasticity in the constituent minerals.

In regions where the upper mantle is clearly the major load-bearing portion of the lithosphere, such as in the ocean basins, low-temperature plasticity of olivine directly influences large-scale processes. These processes include flexure of the lithosphere in response to volcanic loads (Zhong & Watts, 2013), bending of the

lithosphere at subduction zones (Buffett & Becker, 2012; Hunter & Watts, 2016), evolution of stresses at the base of seismogenic faults (Matysiak & Trepmann, 2012), frictional properties of fault gouges (Boettcher et al., 2007), uplift and support of major mountain ranges (England & Molnar, 2015), and formation of new plate boundaries (Thielmann & Kaus, 2012).

Modeling of the large-scale processes mentioned above often relies on constitutive equations describing low-temperature plasticity that are calibrated with laboratory experiments. Early experiments investigating plasticity in olivine were conducted using microindentation (B. Evans & Goetze, 1979), while more recent experiments were performed with a deformation-DIA (D-DIA; Long et al., 2011; Mei et al., 2010; Proietti et al., 2016; Raterron et al., 2004), solid-medium (Griggs) apparatus (Druiventak et al., 2011), high-pressure gas (Paterson) apparatus (Demouchy et al., 2013; Faul et al., 2011), and a variety of micromechanical tests (Idrissi et al., 2016; Kranjc et al., 2016; Kumamoto et al., 2017). Unfortunately, these previous data sets exhibit relatively little agreement. At both laboratory and geological strain rates and at temperatures ranging from 0 to 1000 °C, predictions of the stress olivine is capable of supporting vary by a half order of magnitude (e.g., Figure 1 in Idrissi et al., 2016), which for an exponential flow law at constant stress is equivalent to a variation of many orders of magnitude in strain rate. Significant variability also exists in the ability of these flow laws to predict natural phenomena. For instance, incorporation of the flow law of Mei et al. (2010) in models poorly predicts lithospheric flexure near Hawaii (Watts & Zhong, 2000) yet reasonably well predicts flexure near subduction zones (Hunter & Watts, 2016) and long-term deformation of continental lithosphere (England & Molnar, 2015).

Recently, Kumamoto et al. (2017) proposed a potential explanation for the discrepancy among experimental data sets and for inconsistencies between laboratory and geophysical observations (2017). Based on the results of nanoindentation experiments on single crystals of olivine, these authors demonstrated that the strength of olivine increases with the decreasing size of the contact between the diamond indenter and the sample. This indentation-size effect, well documented in the literature on engineering materials (for a review, see Pharr et al., 2010), is potentially linked to the Hall-Petch effect, whereby yield stress increases with decreasing grain size of a material (Hou et al., 2008; Zhu et al., 2008). Kumamoto et al. (2017) hypothesized that the discrepancy among previous studies resulted primarily from comparing the results from experiments conducted on samples with different grain sizes, a conclusion supported by a compilation and reanalysis of published results taking account of grain size. On this basis, they predicted that olivine with the relatively large grain sizes characteristic of Earth's upper mantle has much lower strength than typically estimated from the results of experiments performed on finer-grained materials. Quantitative links between nanoindentation and deformation of macroscopic samples are difficult to make, however, such that the basic hypothesis that olivine plasticity is dependent on grain size remained untested.

Another potential explanation for the discrepancy among previous results on low-temperature plasticity of olivine is the magnitude of strain at which stress is measured. It is generally recognized that the stress for continued plastic deformation increases significantly over the first several percent of plastic strain. Some authors have calibrated steady state flow laws for olivine plasticity using stresses measured at strains greater than 5–20%, that is, after hardening has occurred and once the stress remains relatively constant (e.g., Druiventak et al., 2011; Long et al., 2011; Mei et al., 2010). In contrast, other authors have calibrated flow laws using stresses measured before significant hardening has occurred. For example, Demouchy et al. (2013) calibrated a relationship between *yield* stress (i.e., the stress at which the macroscopic behavior departs from purely elastic behavior) and strain rate by using the stress at a total strain of 1%. These fundamental differences in which portion of the stress-strain curve was used for calibration lead to significant differences in the resulting constitutive relationships and thus in predictions of flow behavior at geological conditions.

In the present paper, we conducted experiments to characterize the mechanical behavior of olivine aggregates as a function of grain size and strain in order to explain the discrepancies among previous data sets. To eliminate any interexperimental bias that makes it difficult to compare data from different experiments and different studies, we conducted experiments on sample assemblies composed of a stack of two samples of different grain size. This design allows both qualitative and quantitative determination of the relative strength of fine-grained and coarse-grained samples. We use the measured mechanical response of the samples to calibrate a new constitutive model for olivine deforming by low-temperature plasticity that accounts

Table 1
Summary of Unidirectional Deformation Experiments

Experiment #	Position in assembly	Starting materials	Starting grain size (μm)	Pressure (GPa)	Temperature (K)	Strain[a] (%)	Strain rate (10^{-5} s^{-1})	Yield[b] stress (GPa)	Flow stress (GPa)	Stress proxy
San371	Single sample	PI-1519	4.6	7.2–8.4	298	2.4	0.4	3.4	—	Sample
				8.1–8.4	473	5.0	1.0	—	3.7	Sample
				7.0	673	8.0	1.0	—	3.3	Sample
San372	Top	PI-1514	20.0	6.9–9.3	298	1.4	1.2	2.7	—	Bottom
	Bottom	PI-1519	4.6	6.9–9.3	298	2.1	1.2	3.6	—	Sample
San374	Single sample	PI-1514	20.0	8.6–9.2	298	—	1.0	3.5	—	Sample
				8.2–8.7	473	11	1.0	—	3.8	Sample
				7.2–7.4	673	16	1.0	—	3.2	Sample
San375	Top	36	32.9	5.4–9.7	298	2.0	1.9	3.6	—	Sample
				4.4–5.9	873	18	3.0	—	2.5	Sample
					1473	27	3.1	—	0.2	Sample
	Bottom	PT-1166	7.7	5.4–9.7	298	2.5	1.9	4.1	—	Sample
				4.4–5.9	873	18	2.2	—	3.1	Sample
				0.2–1.1	1473	27	5.8	—	0.2	Sample
San376	Top	33	3.0	5.2–9.4	298	2.5	2.0	3.9	4.9	Sample
	Bottom	Aheim	346	5.2–9.4	298	1.3	2.0	2.1	4.9	Top
San377	Top	PT-1166	7.7	5.6–10.1	298	1.7	2.8	3.6	4.3	Sample
	Bottom	PT-1184	42.9	5.6–10.1	298	1.7	2.8	3.2	4.3	Top
San378	Top	[011]c	~700	7.2–10.4	298	1.1	3.6	2.3	4.7	Bottom
	Bottom	34	5.4	7.2–10.4	298	2.2	3.6	3.4	4.7	Sample
San379	Top	34	5.4	5.6–8.5	298	1.8	5.0	3.9	—	Sample
				2.5–4.2	1473	15.0	20.0	—	0.3	Sample
	Bottom	Balsam	334	5.6–8.5	298	1.2	5.0	1.8	—	Top
				2.5–4.2	1473	19.9	10.0	—	0.3	Top
San383	Top	[111]c	~700	5.7– 8.6	298	1.4	4.2	2.6	4.6	Bottom
	Bottom	34	5.4	5.7– 8.6	298	2.0	4.2	3.5	4.6	Sample
San384	Top	PT-1166	7.7	5.9–6.4	298	1.6	3.2	3.0	4.5	Sample
	Bottom	[110]c	~700	5.9–6.4	298	2.2	3.2	2.5	4.5	Top

[a]Strain at which stress is reported. [b]Yield stresses are only given for room-temperature tests. Flow stresses are listed for experiments at high temperature since yield was not detectable.

for grain size and strain. Not only does this new model explain the discrepancies among previous results, but it helps to explain disagreement among several recent large-scale geophysical measurements that yield estimates of lithospheric strength.

2. Methods

2.1. Sample Preparation

Aggregates and single crystals of olivine provided starting materials for the experiments (Tables 1 and 2). Aggregates consisted of either hot-pressed powders of San Carlos olivine or natural dunites. Hot-pressed aggregates were synthesized from powders of San Carlos olivine containing ~1% orthopyroxene to buffer the silica activity. Powders were initially dried for 10 hr in a gas-mixing furnace at 1000 °C and an oxygen fugacity near 10^{-7} Pa. Powders were uniaxially pressed into a Ni jacket at room temperature. Jacketed pellets were then hot pressed in a gas-medium apparatus (Paterson, 1990) at 1250 °C for 3 to 60 hr. Longer annealing times produced samples with coarser mean grain sizes. Several samples (starting material PI-1514 and PI-1519) were deformed in a gas-medium apparatus as part of the data set presented by Hansen et al. (2011). Natural dunites consisted of samples from Åheim, Norway, and Balsam Gap, North Carolina. Cores 1 cm in diameter were dried in a gas-mixing furnace following the same procedure used for olivine powders. In addition to olivine, these natural dunites contain ~2% orthopyroxene, ~2% serpentine, and ~2% spinel. Several samples consisted of single crystals of San Carlos olivine, which were hand selected to be free of visible cracks and inclusions.

All samples were cored with a diamond coring drill to produce right-cylindrical samples, as illustrated in Figure 1. Samples were ground to 0.55 ± 0.05 mm in length except for San371, San374, San386, and

Table 2
Summary of Cyclical Deformation Experiments

Experiment #	Cycle	Position in assembly	Starting materials	Starting grain size (microns)	Pressure (GPa)	Temperature (K)	Strain rate (10^{-5} s^{-1})	Yield stress (GPa)	Flow stress (GPa)	Back stress (GPa)	Stress proxy
San382	1	Top	[111]c	~700	5.3–8.2	298	2.7	2.5	4.3	—	Bottom
	2					298	2.7	−0.2	−3.8	1.8	
	1	Bottom	33	3.0	5.3–8.2	298	2.7	3.8	4.3	—	Sample
	2					298	2.7	−0.7	−3.8	1.6	
San385	1	Bottom	PT-1166	7.7	5.8–7.7	298	7.1	3.0	4.6	—	Sample
	2					298	−3.9	−0.2	−4.4	2.1	
	3					298	7.1	1.7	5.5	1.9	
	4					298	−3.9	−1.1	−5.0	1.9	
	5					298	7.1	1.8	4.9	1.6	
	6					298	−3.9	−1.3	−5.1	1.9	
	1	Top	[011]c	~700	5.8–7.7	298	7.1	2.1	4.6	—	Bottom
	2					298	−3.9	−0.3	−4.4	2.0	
	3					298	7.1	1.8	5.5	1.8	
	4					298	−3.9	−0.9	−5.0	2.0	
	5					298	7.1	1.4	4.9	1.7	
	6					298	−3.9	−1.6	−5.1	1.7	
San386	1	Single sample	33	3.0	5.1–8.2	298	11.6	3.3	5.3	—	Sample
	2					298	−6.0	−0.8	−4.1	1.7	
	3					298	11.6	2.5	5.1	1.3	
	4					298	−6.0	−1.3	−4.8	1.8	
San388	1	Single sample	34	5.4	4.1–7.1	873	3.7	1.2	2.7	—	Sample
	2					873	−1.9	0.0	−2.8	1.4	
	3					573	4.9	1.4	3.5	—	
	4					573	−2.8	−0.3	−3.5	1.6	
	5					298	6.3	1.8	4.5	—	
	6					298	−4.5	−0.6	−4.1	1.7	
San389	1	Top	PT-1166	7.7	5.0–7.2	873	9.8	1.5	3.0	—	Sample
	2					873	−6.4	0.0	−3.1	1.6	
	3					298	13.7	2.9	4.6	0.8[a]	
	1	Bottom	[011]c	~700	5.0–7.2	873	9.8	1.3	2.7	—	
	2					873	−6.4	0.2	−2.8	1.5	Top
	3					298	13.7	2.9	4.6	0.8[a]	

[a]Samples were annealed at 1000 °C before reloading in the final cycle.

San388, which were ground to 1.1 ± 0.1 mm in length. Previously deformed samples (PI-1514 and PI-1519, see above) were cored parallel to the previous loading direction. Single crystals were cored along an axis that (1) bisects the [001] and [010] crystallographic directions, (2) bisects the [100] and [010] directions, or (3) is equally spaced between the [100], [010], and [001] directions. These directions correspond to the $[011]_c$, $[110]_c$, $[111]_c$ orientations, respectively, following the nomenclature of Durham and Goetze (1977) in which the subscript "c" indicates a cubic reference frame. These orientations were chosen to maximize the resolved shear stress on the (010)[001], (010)[100], and {110}[001] slip systems, respectively. The first two slip systems are active in olivine over a wide range of deformation conditions (e.g., Phakey et al., 1972; Bai et al., 1991; Durham & Goetze, 1977), and the latter is active especially at low temperatures (Phakey et al., 1972).

A schematic diagram of a sample assembly is presented in Figure 1. For most experiments, two samples of different grain size, one stacked on top of the other, were surrounded at top and bottom by dense alumina pistons and machinable alumina pistons. Discs of Ni foil placed between the two olivine samples and on either end of the dense alumina pistons served as strain markers in radiograph images during deformation. Olivine samples were also wrapped with Ni foil to track the vertical edges of the samples during deformation. The stack of samples and pistons was contained in concentric sleeves of MgO and graphite, the first to act as a pressure medium and the second to act as a resistive furnace. This cylindrical assembly was contained inside a mullite sphere with a cylindrical bore through its center. The mullite sphere was centered within

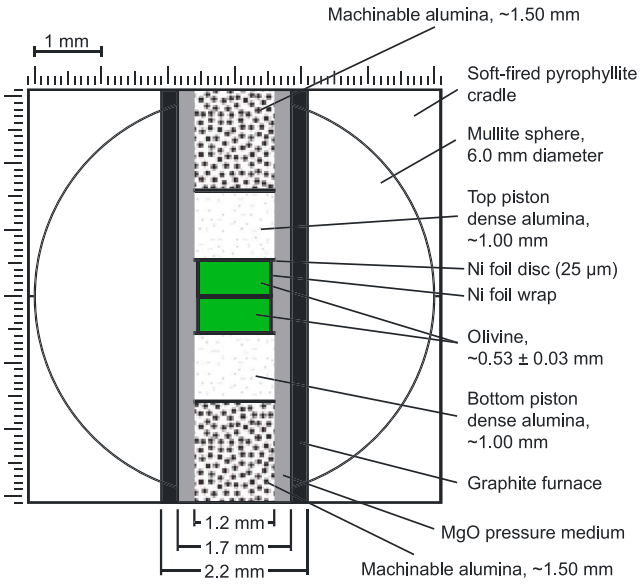

Figure 1. Schematic illustration of the sample assembly and pressure medium. An assembly with a stack of two samples is depicted. Single sample assemblies contained a sample of length equivalent to the sum of the lengths of the two samples shown here.

a pyrophyllite cube. Sample assemblies did not include a thermocouple. For annealing steps at elevated temperature prior to deformation (see below), and for the few runs not conducted at room temperature, the temperature was determined from calibrated relationships between heater power and temperature. The thermocouple-free approach to temperature control avoids degrading the mechanical stability of the sample assembly and is at least as accurate as operating with a thermocouple (Dixon & Durham, 2018).

2.2. Deformation Experiments

Deformation experiments were conducted in a D-DIA housed on the 6-BM-B beamline at the Advanced Photon Source at Argonne National Laboratory. A synchrotron X-ray source was employed to measure strain directly through radiography and to determine the stress state directly through X-ray diffraction. The sample assembly was contacted by a hydraulically loaded anvil on each cube face. Pressurization from the main loading ram applied a load to all anvils simultaneously, generating a positive mean stress, while advancement or retraction of the vertical anvils produced a differential stress (Durham et al., 2009; Mei et al., 2010; Wang et al., 2003; Weidner et al., 2010).

Axial strain of the sample column was measured with successive radiographs throughout each deformation experiment. The position of each Ni-foil marker was tracked between successive radiographs using image cross correlation. A peak-interpolation algorithm allowed subpixel resolution in determining the location of peaks in the correlation function, resulting in a strain resolution between 10^{-5} and 10^{-4}. Strain was calculated as the true (logarithmic) strain in the vertical direction and was measured separately for each sample in assemblies containing two samples (hereafter referred to as two-sample assemblies).

Pressure and differential stress were derived using energy-dispersive X-ray diffraction and a white X-ray source. Diffraction patterns were collected from olivine samples at intervals as long as 5 min to as brief as 15 s throughout the deformation experiment. As described in Weidner et al. (2010), detectors are arrayed downstream of the sample at a variety of azimuths around the horizontal incident beam, at an angle of ~6.5° to the beam direction. Collimation of the beam to 6.5° ensures that diffracted X-rays arriving at the detectors are diffracted only by the sample and not other portions of the sample assembly. Each energy peak in a diffraction spectrum corresponds to a (*hkl*) plane whose spacing, d_{hkl}, can be calculated using Bragg's law and the fixed diffraction angle near 3.25°. This angle is precisely calibrated for each detector at least once every five experiments using a powdered alumina standard. For olivine, the primary diffracting planes used were (*hkl*) = (130), (131), and (112). To analyze pressure and differential stress at high frequency in near real time, we used only 2 of the 10 available X-ray detectors, one at the vertical azimuth relative to the incident beam and the other at the horizontal azimuth, detecting diffracted X-rays from planes oriented nearly perpendicular and nearly parallel to the maximum principal stress, respectively. Using only two detectors relies on the assumption that any anisotropy in stress has a vertical symmetry axis. Peaks were chosen using the *peakfit* function for MATLAB® (O'Haver, 2018, pp. 340–358), fitting the (130) peak with a single Gaussian and the doublet containing the (112) and (131) peaks with two equal-width Gaussians. The *d* spacings measured with these two detectors were used to estimate the vertical and horizontal lattice strains, respectively. The *d* spacing due to the pressure was calculated as

$$d_p = \frac{d_v + 2d_h}{3}, \tag{1}$$

where d_v is the *d* spacing measured from the detector at the vertical azimuth and d_h is the *d* spacing measured from the detector at the horizontal azimuth.

Reported pressures were calculated using the position (130) peak. Unit-cell volume (*V*) was calculated as

$$V = \left[d_p\left(h^2 + k^2 + l^2\right)^{1/2}\right]^3. \quad (2)$$

A third-order Birch-Murnaghan equation of state for olivine was then used to calculate pressure (mean stress) as

$$P = \left(\frac{3K_0\left(1 + K_T{}'\right)}{2}\right)\left[\left(\frac{V_{0,T}}{V}\right)^{\frac{7}{3}} - \left(\frac{V_{0,T}}{V}\right)^{\frac{5}{3}}\right]\left\{1 + \frac{3}{4}\left(K_P{}' - 4\right)\left[\left(\frac{V_{0,T}}{V}\right)^{\frac{2}{3}} - 1\right]\right\}, \quad (3)$$

where K_0 is the bulk modulus of olivine and K_T' and K_P' are its temperature and pressure derivatives, respectively. These parameters were taken from Abramson et al. (1997) and Kumazawa and Anderson (1969). $V_{0,T}$, the volume of the unit cell at room pressure and the temperature of the experiment, is calculated as

$$V_{0,T} = V_0 \exp\left(2.55\text{E}{-5}\ \left(T - T_0\right) + \frac{1}{2}\ 1.15\text{E}{-8}\ \left(T^2 - T_0^2\right)\right) \quad (4)$$

using the thermal expansivity of olivine measured by Suzuki (1975).

Lattice strains were converted to stresses as

$$\sigma_d = \left(\frac{1}{2G_R}\right)^{-1}\ \frac{d_h - d_v}{d_p}. \quad (5)$$

G_R is the X-ray shear modulus calculated assuming the Reuss (isostress) condition using the formulation of (Singh et al., 1998) and elastic constants from Abramson et al. (1997), which includes pressure derivatives at room temperature, and from Isaak (1992), which includes temperature derivatives at room pressure. The difference between the stress measured in the vertical direction and that measured in the horizontal direction is taken to be the differential stress. We report compressive stresses as positive and tensile stresses as negative. A differential stress was calculated for each of the three diffraction peaks. To define the stress at any given strain, we average the stresses estimated from each diffraction peak, resulting in an uncertainty that depends on the stress heterogeneity within the sample. During initial elastic loading, the stress uncertainty is on the order of 100 MPa, whereas after substantial plastic strain at room temperature, the uncertainty is on the order of 1 GPa. Measured yield stresses, by definition, correspond to portions of the experiment prior to any plastic deformation (see below) and therefore are subject to the smaller of these uncertainties. In experiments with two samples, the stress was measured in the finer-grained sample, which yields better diffraction patterns due to the comparatively larger number of grains per diffraction volume; the stress was assumed to be the same in the coarser-grained sample. For one experiment with two samples (San375), stresses measured in both the top and bottom samples were within error of each other.

Stress and strain were computed nearly continuously in real time during each experiment. For most experiments, mechanical data were collected during initial pressurization, which aided in maintaining an approximately hydrostatic stress state. Once at the test pressure, the temperature was increased to ~1000 °C for 20–60 min to relax any internal stress heterogeneity in the samples. Stress relaxation was monitored with the diffraction data. After the heterogeneity in the nonhydrostatic internal stress ceased to relax further, samples were quenched to room temperature. Next, the vertical rams were advanced at a rate controlled with hydraulic syringe pumps to produce a strain rate, averaged over the samples, that was constant within a factor of 2. Average strain rates within olivine samples ranged from 2×10^{-5} to 2×10^{-4} s^{-1}. In all experiments, the differential stress was less than the confining pressure (here defined as the horizontal stress), confirming that brittle processes were suppressed according to Goetze's criterion (Kohlstedt et al., 1995). For several samples, the temperature was subsequently increased, and the corresponding decrease in differential stress was monitored. For another subset of samples, after initial yield, the motion of the vertical anvils was reversed to generate negative strain rates until the differential stress changed sign and the sample yielded in the reverse direction in tension. This procedure was repeated over multiple cycles, allowing yield to be observed in both the forward and reverse directions in a single experiment. At the end of experiments, the vertical anvils were withdrawn until the differential stress was approximately 0, after which the pressure from the main loading rams was decreased while adjusting the position of the vertical anvils to maintain a roughly hydrostatic stress state. Details of all deformation experiments are included in Tables 1 and 2.

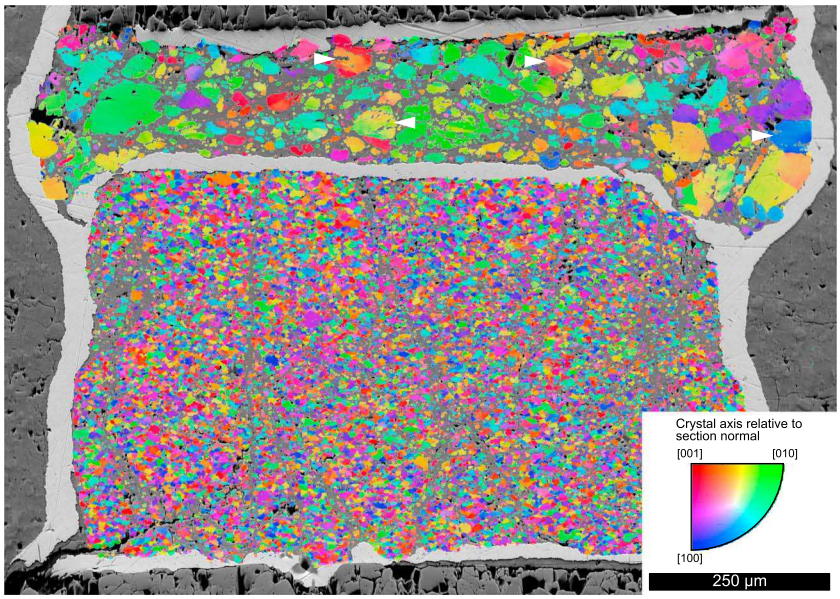

Figure 2. Sample assembly from San372 after deformation. A semitransparent electron backscatter diffraction map is superimposed on a forescattered-electron image. Color scale indicates the orientation of the normal to the plane of section relative to the crystal axes. White arrows indicate examples of grains with observable lattice curvature.

2.3. Microstructural Analysis

Samples were analyzed with a scanning electron microscope to determine mean grain sizes before and after deformation experiments. Prior to the experiments, we analyzed the starting microstructure in the sample material directly adjacent to the location of the sample cores, on surfaces normal to the eventual loading direction. After the experiments, the sample assemblies were recovered from the graphite furnace inward, and we analyzed the microstructures of the samples on surfaces parallel to the loading direction. For both starting and deformed samples, material was impregnated with epoxy resin and then ground using a diamond grinding wheel. Ground surfaces were then polished with diamond slurries of progressively finer grit, eventually reaching a grit size of 0.05 μm. Polished samples were analyzed with an FEI Quanta 650 scanning electron microscope equipped with a field emission gun in the Department of Earth Sciences at the University of Oxford. We mapped microstructures with electron backscatter diffraction (EBSD) using an Oxford Instruments Nordlys Nano EBSD camera and AZtec software package. In general, successful indexing solutions were found for >80% of all pixels. EBSD maps were postprocessed to remove isolated pixels disparate from their neighbors by >10°. Pixels for which an orientation was not obtained and with at least six indexed neighbor pixels were filled with the average orientation of those neighbors. Mean grain size was estimated using the linear intercept method and applying a scaling factor of 1.5 (Underwood, 1970, pp. 80–93). Grain boundaries were defined by misorientation angles >10°.

3. Results

3.1. Sample Microstructures

The grain size for all samples was measured prior to deformation, with values of mean grain size presented in Tables 1 and 2. The EBSD map in Figure 2 reveals that the coarse-grained sample at the top has undergone significantly more vertical shortening than the fine-grained sample on the bottom. This difference in the amount of deformation for samples of different grain size is consistent with the mechanical data presented in the next section. Most grains exhibit measurable gradients in crystallographic orientation, which are most easily observed in the coarse-grained sample in Figure 2. These orientation gradients are likely the result of accumulations of geometrically necessary dislocations (GNDs; Wallis et al., 2016). EBSD indexing was generally poor near grain boundaries. Several small test maps revealed that the indexing rate in these regions increased if longer exposure times were used when collecting diffraction patterns. This dependence on

exposure time suggests that unindexed regions are the result of locally high lattice distortion, again due to significant accumulations of GNDs.

3.2. Mechanical Results

3.2.1. Unidirectional Deformation Experiments at Room Temperature

Mechanical data from experiments on samples loaded unidirectionally are presented as stress-strain curves in Figure 3. Most samples (excluding San371 to San374) exhibited a linear relationship between stress and strain during initial loading. The slope of the loading curve indicates an elastic modulus of ~200 GPa, consistent with the average Young's modulus of olivine measured by other techniques (e.g., Abramson et al., 1997). All experiments reveal a distinct yield point associated with a departure from a linear relationship between stress and strain, which was observable in the stress-strain curves for both samples in the two-sample experiments.

Stresses determined from different diffraction peaks agree to within ~100 MPa at low strain, with increasing disagreement at higher strains. All samples strain hardened after yielding. Post-deformation microstructural analysis revealed that the relatively few grains in the coarse-grained sample of San379 were oriented such that very little stress was resolved on available slip systems, so data associated with this sample were not considered in subsequent analyses.

3.2.2. Grain Size Dependence of Deformation in Two-Sample Assemblies

Tracking the strain in both samples of a two-sample assembly allows determination of the relative strength of the samples. Strain is presented as a function of time for all unidirectional experiments in Figure 4. For experiments with two samples, the coarser-grained sample is always weaker. That is, the black points representing data from coarser-grained samples always achieve larger strains than the red points representing data from finer-grained samples.

In addition to qualitative determination of relative sample strengths, data from experiments with two samples offer a special advantage in quantitatively determining the yield stress. Yield stress is difficult to determine in a precise manner because it requires identification of a break in slope on a stress-strain diagram, for which real data often exhibit smoothly varying slopes rather than a distinct breakpoint. As depicted schematically in Figure 5, the response of a stacked sample allows the yield point to be precisely determined from a plot of strain versus time. During initial elastic loading, if both samples have approximately the same elastic moduli, they will exhibit the same strain increase with increasing time. However, when the weaker sample yields, it will begin to deform at a proportionally faster rate than the stronger sample, which is still deforming elastically. In fact, the stronger sample will not exhibit any further deformation unless the weaker sample strain hardens. The point of divergence in the strain-time curves for the two samples marks the plastic yield of the weaker sample. As evidenced in Figure 4, all two-sample experiments exhibit a clear divergence in the strain-time curves. Once the stronger sample yields, both strain-time curves will exhibit another change in slope. For low-temperature plasticity, in which there is little dependence of the stress on strain rate, the two samples will then exhibit approximately the same strain rate, matching the macroscopic strain rate.

We use yield stresses determined in this manner to evaluate the grain size dependence of yield. All measured yield stresses are presented in Tables 1 and 2. Figure 6 specifically compares the yield stresses measured at room temperature in coarse-grained samples to those of their fine-grained counterparts in the same assembly. For all experiments on two-sample assemblies, the coarse-grained sample yields at lower stresses than the fine-grained sample. Fine-grained samples are stronger at yield than coarse-grained samples by a factor of 1.20 to 1.25.

3.2.3. Unidirectional Deformation Experiments at High Temperature

For unidirectional experiments at elevated temperatures, temperature was only increased after yield had occurred during the initial room-temperature deformation experiment. Thus, yielding behavior was not observed at high temperatures. Therefore, we refer to the final stress at the end of these experiments as the *flow stress*. As illustrated in Figure 3, the flow stress generally decreases with increasing temperature, as expected for thermally activated deformation mechanisms. After an increase in temperature, an initial relaxation occurs in which the flow stress gradually decreases. This relaxation is most evident at higher temperatures. At temperatures up to 873 K, strain hardening still takes place. Tests conducted at 1473 K (e.g., within San375 and San379) do not exhibit strain hardening.

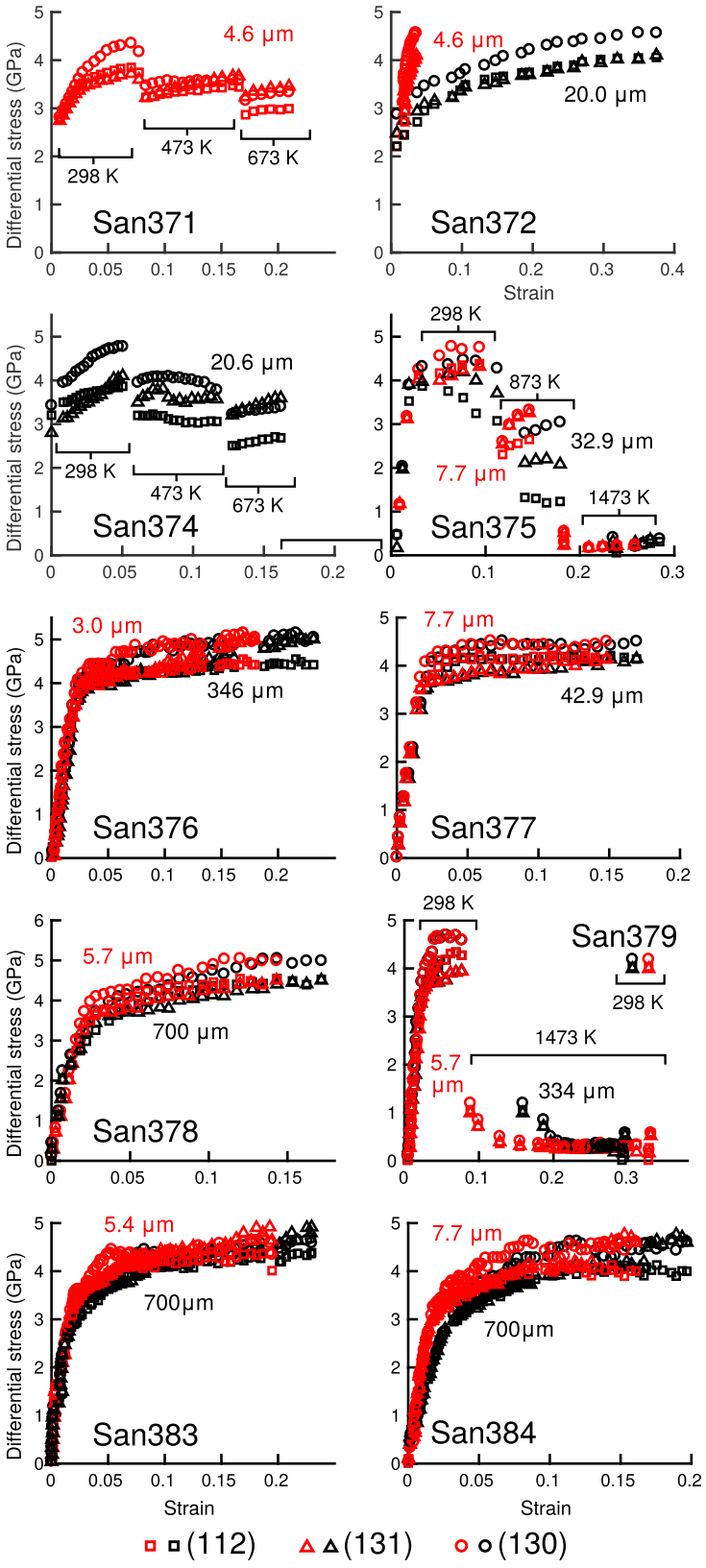

Figure 3. Stress as a function of strain in unidirectional experiments. Red points indicate data from fine-grained samples. Black points indicate data from coarse-grained samples. Unless otherwise noted, the temperature during deformation was 298 K. The legend at the bottom identifies the diffraction peaks used to calculate stresses.

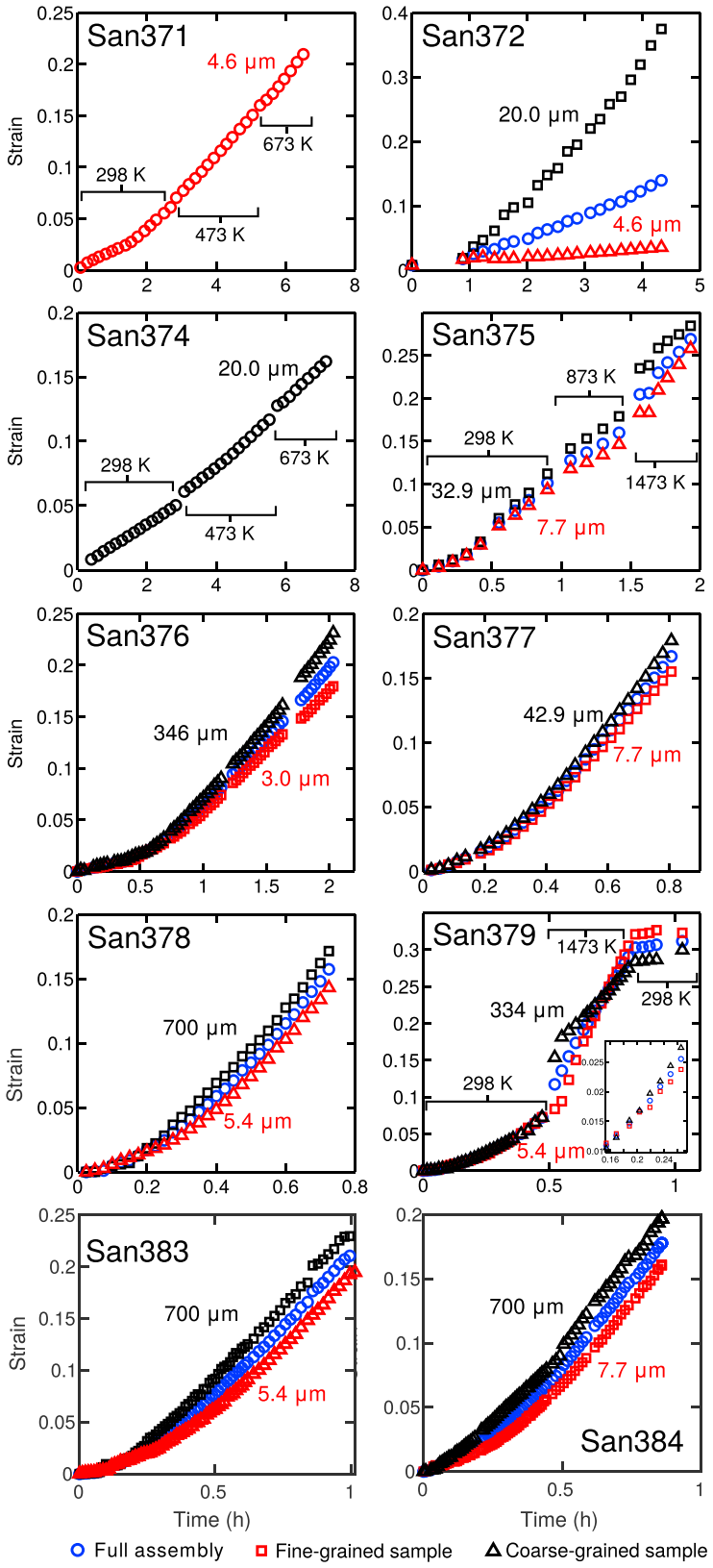

Figure 4. Strain as a function of time for unidirectional experiments. Red points indicate data from fine-grained samples. Black points indicate data from coarse-grained samples. Unless otherwise noted, the temperature during deformation was 298 K. For two-sample assemblies, the blue points indicate the total strain averaged over both samples.

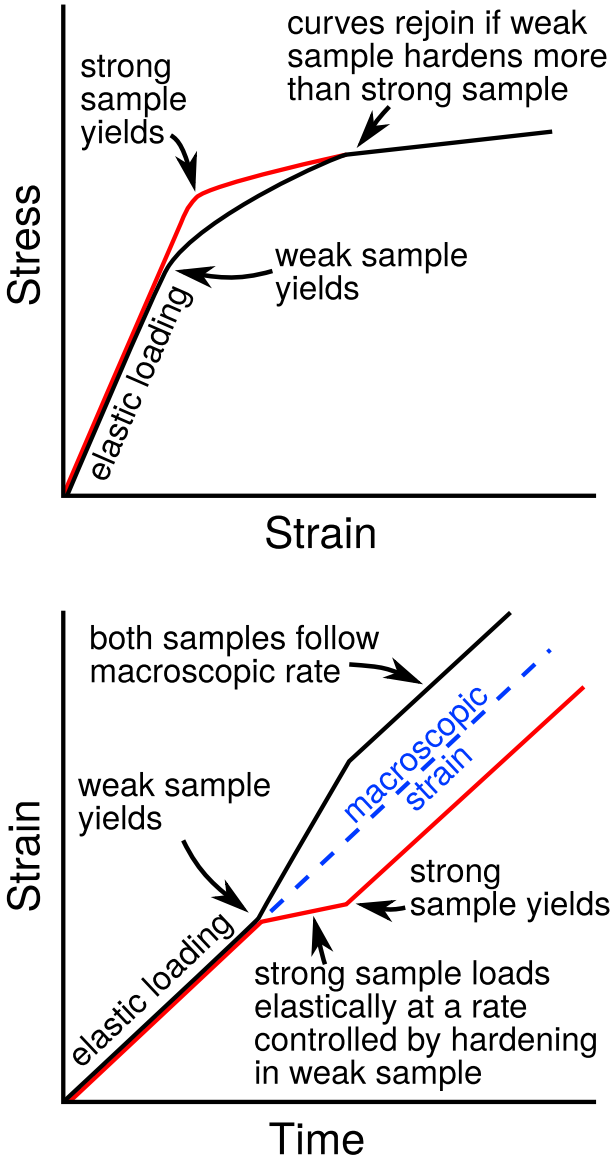

Figure 5. Schematic depicting the determination of the yield point in a two-sample assembly. (top) Typical stress-strain curves for two samples with different yield points. With real data, some ambiguity is generally involved in determining the exact point of yield from stress-strain curves. (bottom) Strain-time curves for the same samples, illustrating the divergence between curves for the weak and strong samples. The point of divergence indicates the strain at which the weaker sample yielded.

In two experiments (San375 and San379), we observed a reversal in relative strength of the two samples with increasing temperature. This transition is most evident in the strain-time curves presented in Figure 4. During the initial room-temperature portion of the experiment, the coarser-grained sample yields at a lower stress than the fine-grained sample (see inset for San379 in Figure 4). However, at 1473 K for both experiments, the finer-grained sample exhibits a faster strain rate than the coarse-grained sample, leading to a crossover of the two strain-time curves. Thus, finer-grained samples are weaker than coarse-grained samples at high temperature, consistent with the operation of grain-size sensitive creep (e.g., G. Hirth & Kohlstedt, 1995; Hansen et al., 2011). The flow law for dislocation-accommodated grain boundary sliding from Hansen et al. (2011) predicts strain rates for the stresses and grain sizes of experiments San375 and San379 at 1473 K that are within factors of 6 and 2, respectively, of the observed strain rates.

3.2.4. Cyclical Deformation Experiments

Consistent with our unidirectional tests, cyclical tests also demonstrate that (1) on initial loading, coarser-grained samples yield before finer-grained samples and (2) with increasing deformation, all samples strain harden significantly until an approximately steady state flow stress is reached, which is around 4 to 5 GPa for samples deformed at room temperature, regardless of grain size. The mechanical data from cyclical tests are presented in Table 2 and Figure 7. Yield stresses from the first loading cycle are also presented in Figure 6. On unloading, both samples exhibit elastic behavior with an apparent modulus identical to that observed during the initial loading segment. With increasingly negative differential stress, both samples eventually yield in the reverse direction (i.e., toward negative strains). Again, the coarse-grained sample always yields before the fine-grained sample, and strain hardening progresses until stresses of approximately −4 to −5 GPa are reached. After the first cycle, this basic pattern is repeatable regardless of the number of imposed loading cycles.

A distinct history dependence is observed in the yield behavior during cyclical experiments. As is evident in Table 2, after the first loading path, subsequent loading in the reverse direction results in yield at a much lower absolute value of stress than for the initial yield. This lower value of the yield stress continues for all subsequent loading cycles. For example, the bottom sample of San385 initially yielded at 4.0 GPa but yielded during subsequent cycles at values between 1.0 and 3.3 GPa.

Several cyclical experiments were conducted in which the temperature was changed between cycles (Figure 7). For San388, the temperature was initially 600 °C and was progressively decreased after each cycle. Both the yield stress and the maximum flow stress increased with decreasing temperature. For San389, the temperature was also initially elevated and progressively decreased after each cycle. Both the yield stress and the maximum flow stress decreased with increasing temperature. Notably, prior to the final, room-temperature cycle of San389, deformation was arrested and the temperature was elevated to 1000 °C for 10 min, while stresses were observed to relax. Upon reloading at room temperature, the yield in this final cycle was not reduced but instead was comparable to those observed on initial loading of other samples with similar grain sizes.

4. Discussion

The experiments presented here reveal four key phenomena in low-temperature plasticity of olivine. (1) The yield strength of olivine aggregates depends on grain size, (2) the yield strength decreases with increasing

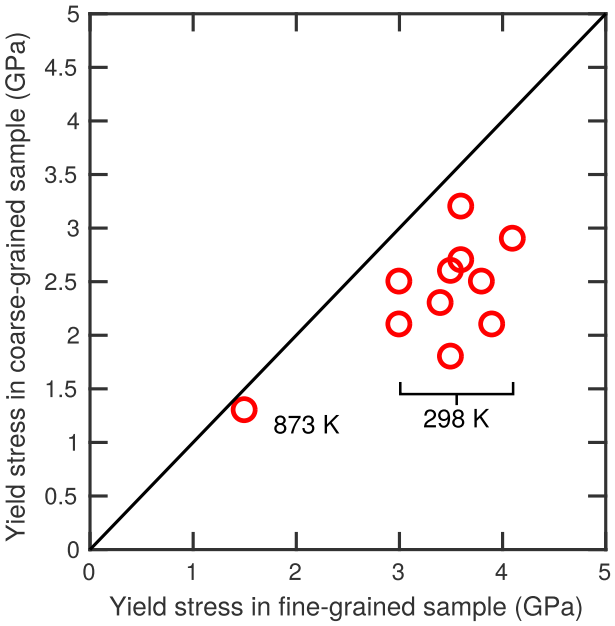

Figure 6. Comparison of yield stresses for coarse-grained and fine-grained samples in the same assembly. The black line indicates equal yield stresses for the two samples.

temperature, (3) significant strain hardening occurs until an approximate steady state flow stress is reached that is independent of grain size, and (4) the yield stress in cyclical loading tests decreases after the first deformation cycle. Based on these observations, we explore the underlying microphysical processes involved in olivine plasticity and develop a constitutive model for application to deformation of the lithospheric mantle.

4.1. Rate-Limiting Processes in Low-Temperature Plasticity

Low-temperature plasticity can be characterized by a flow law that encapsulates the dependence of strain rate on temperature, stress, and the intrinsic resistance to the motion of dislocations. Most flow laws for plasticity begin with the Orowan equation, for which the strain rate is given by

$$\dot{\gamma} = \rho_m b v, \tag{6}$$

where $\dot{\gamma}$ is the shear strain rate, ρ_m is the mobile dislocation density, b is the magnitude of the Burgers vector, and v is the dislocation velocity. The velocity can be limited by *local interactions* of dislocations with lattice-scale obstacles (e.g., the intrinsic atomic structure, precipitates, or other dislocations) or by *long-range interactions* with the stress fields generated by arrays of dislocations. Dislocation velocity is generally described by

$$v = \alpha f b \exp\left(-\frac{\Delta G}{RT}\right), \tag{7}$$

where α is a geometrical factor, f is the attempt frequency for the dislocation to cross the barrier to its motion, R is the gas constant, T is temperature, and ΔG is the Gibbs free energy. In the presence of a stress field, the Gibbs free energy can be decomposed into $\Delta G = \Delta F - \tau \Delta V$ (A. G. Evans & Rawlings, 1969), where ΔF is the Helmholtz free energy (herein referred to as the activation energy), ΔV is the activation volume, τ is the shear stress resolved on the dislocation slip system, and $\tau \Delta V$ is the work carried out by the stress field. The term ΔV is often taken to be equal to $\Delta F/\Sigma$, where Σ is a measure of the height of the energy potentials associated with local barriers that must be overcome for the dislocation to glide (i.e., the glide resistance at 0 K). Thus, equation (7) can be rewritten and combined with equation (6) to yield

$$\dot{\varepsilon} = A \exp\left(-\frac{\Delta F}{RT}\right) \exp\left(\frac{\Delta F}{RT}\frac{\sigma}{\Sigma}\right), \tag{8}$$

where $A = \alpha \rho_m b^2 \nu$. Note that equation (8) uses the uniaxial stress and strain rate, σ and $\dot{\varepsilon}$, instead of the shear stress and strain rate; the geometrical factor for converting between the two is absorbed in α. The value of A is a function of stress because the mobile dislocation density is stress dependent, but this contribution to the overall dependence of strain rate on stress is minor relative to the exponential term; therefore, we treat A as a phenomenological constant. The form of equation (8) assumes that the energy potentials of the barriers are, on average, shaped like a box (Kocks et al., 1975 section 24). To account for arbitrarily shaped potentials that likely arise if the barrier to motion is the intrinsic resistance of the atomic structure of the lattice (i.e., the lattice friction), Kocks et al. (1975, 141) modified this equation to

$$\dot{\varepsilon} = A \exp\left\{-\frac{\Delta F}{RT}\left[1-\left(\frac{\sigma}{\Sigma}\right)^p\right]^q\right\}, \tag{9}$$

where p and q are constants that depend on the shape of the potential. If the primary barrier to motion is lattice friction, then Σ is often referred to as the Peierls stress. Jain et al. (2017) noted that extrapolations of olivine flow laws to geological conditions depend strongly on p and q, and unfortunately these parameters are difficult to constrain experimentally. However, throughout much of the metallurgical literature, p and q are simply taken as unity a priori, since the primary barrier to yield is often local dislocation interactions, which are best described with a box-shaped potential if they are regularly spaced, discrete obstacles (Frost & Ashby, 1982, section 2.2). We adopt this assumption for olivine since, as described in the next section,

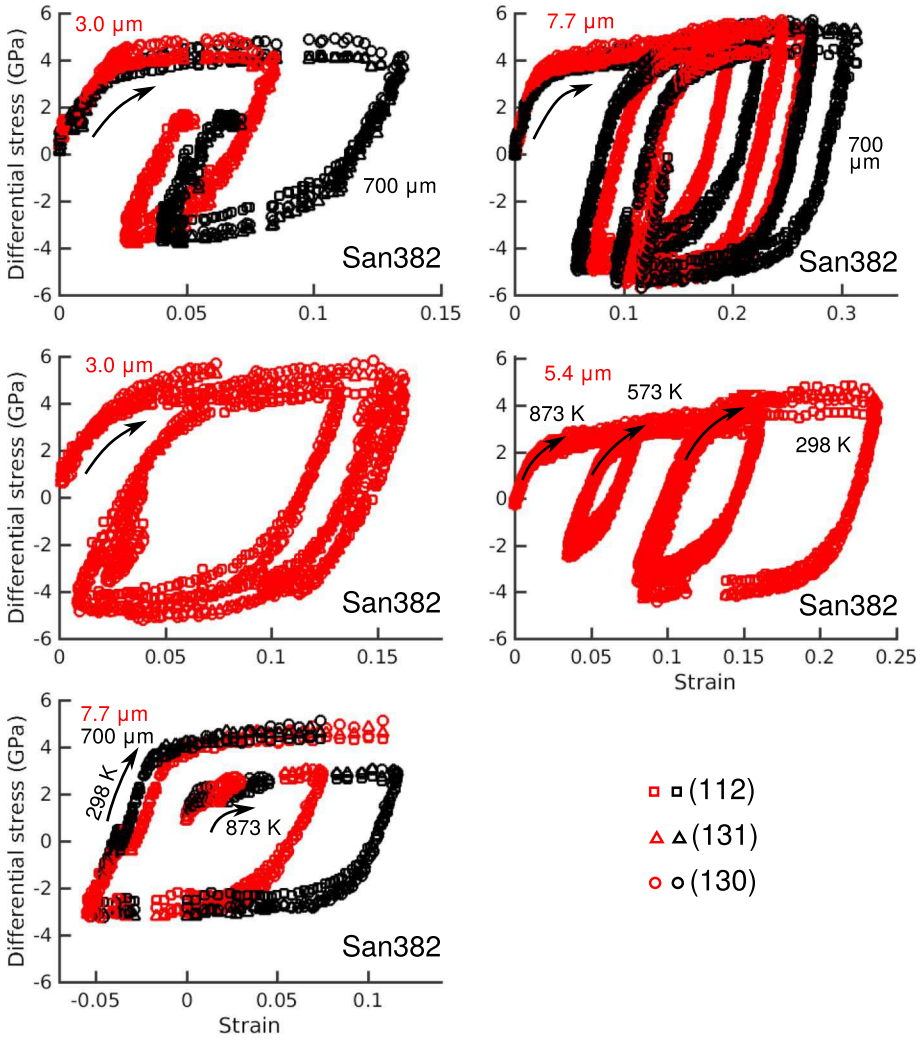

Figure 7. Stress as a function of strain for cyclical experiments. Red points indicate data from fine-grained samples. Black points indicate data from coarse-grained samples. Arrows indicate the direction of loading. Positive values of stress are compressive. Unless otherwise noted, the temperature during deformation was 298 K. The legend indicates the diffraction peaks used to calculate stress.

we suggest that the most important local barriers to dislocation motion at yield are discrete obstacles rather than lattice friction.

Long-range interactions also affect the dislocation velocity. Arrays of dislocations can result in a nonnegligible net Burgers vector that will have an associated long-range stress field (e.g., Bayley et al., 2006; Harder, 1999). Because this stress field can work against the macroscopically applied stress, it is often referred to as a back stress, σ_b, which acts to reduce the effective stress driving dislocation motion and leads to a flow law of the form

$$\dot{\varepsilon} = A \exp\left(-\frac{\Delta F}{RT}\right) \sinh\left(\frac{\Delta F}{RT}\frac{\sigma-\sigma_b}{\sum}\right). \tag{10}$$

Note that here we replace the second exponential in equation (8) with a hyperbolic sine following Garofalo (1963) to allow the strain rate to be negative if the effective stress, $\sigma - \sigma_b$, is negative. That is, if the back stress exceeds the applied stress, then reverse flow can occur.

Equation (10) can be solved for the applied stress,

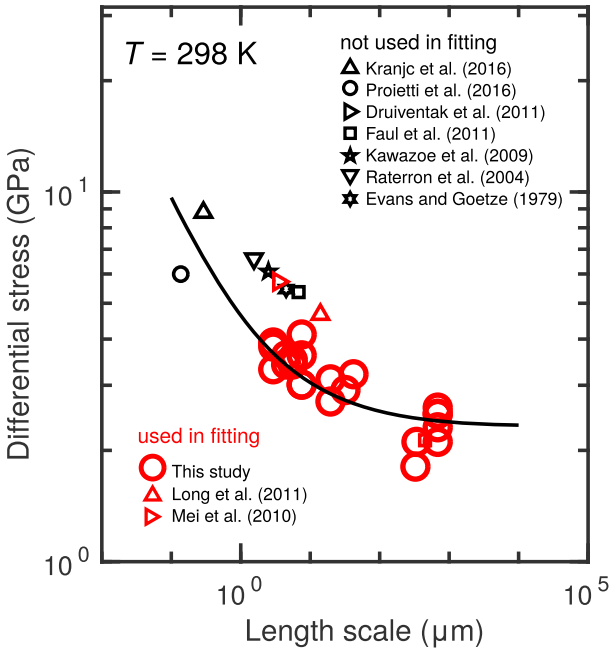

Figure 8. Yield stress as a function of grain size at room temperature. Results from this study (large red circles) are compared to extrapolation of flow laws from previously published results to room temperature. Grain size is taken as the relevant length scale for experiments on olivine aggregates. The contact radius is taken as the relevant length scale for indentation experiments. The solid line is obtained from the calibrated model discussed in section 4.4.

$$\sigma = \frac{RT\sum}{\Delta F}\sinh^{-1}\left[\frac{\dot{\epsilon}}{A}\exp\left(\frac{\Delta F}{RT}\right)\right] + \sigma_b \ , \tag{11}$$

which highlights the relationships among temperature and local and long-range interactions. The first term on the right-hand side represents the stress supported by local interactions, which is a clear function of T as well as Σ. The second term represents the stress supported by long-range interactions, which is purely elastic in nature and therefore independent of T, aside from the small effect of T on the elastic moduli.

4.2. Grain Size Sensitivity of the Yield Stress

Our results demonstrate that the yield stress of olivine at low temperatures is a function of grain size. This result is consistent with the work of Trepmann et al. (2013). In Figure 8, we have compiled estimates of yield strength from previously published deformation experiments on olivine. Following Kumamoto et al. (2017), we compare our results to previously published results as a function of the characteristic length scale of deformation, taken to be the grain size for experiments on polycrystals and the contact radius for indentation experiments. To compare data from our room-temperature experiments to previous data from experiments at higher temperature, we have extrapolated previously published flow laws to room temperature and calculated the stress. General consistency exists among these data sets demonstrating that smaller characteristic length scales lead to higher yield stresses. This agreement also suggests that similar mechanisms lead to the dependence of strength on grain size and to the dependence of strength on contact radius, consistent with compilations of existing metallurgical literature (Dunstan & Bushby, 2014; Li et al., 2016).

Because of its relevance to engineering and materials design, significant work has been conducted on grain size effects in plasticity. Recent reviews can be found in Li et al. (2016) and Cordero et al. (2016). Strengthening with decreasing grain size is generally referred to as the Hall-Petch effect (Hall, 1951; Petch, 1953). Many mechanistic models have been proposed to explain the Hall-Petch effect through the interaction of mobile lattice dislocations with other aspects of the microstructure. Proposed barriers to dislocation motion include (1) the strength of grain boundaries at the head of a dislocation pileup (Hall, 1951; Petch, 1953), (2) the difficulty in emitting lattice dislocations from grain boundaries because of interactions with grain boundary dislocations (Bata & Pereloma, 2004), (3) forest dislocations produced through emission from grain boundaries (J. Li, 1963), (4) GNDs produced as a result of elastic incompatibility (Meyers & Ashworth, 1982), (5) GNDs produced as a result of plastic incompatibility (Ashby, 1970), (6) dislocations generated during strain hardening, whose density depends on grain size (Conrad, 1963; Conrad et al., 1967), (7) the operation of a Frank-Read source in a neighboring grain as a result of the stress fields ahead of a dislocation pileup (e.g., Armstrong et al., 1962; Cottrell, 1953; Smith & Worthington, 1964), and (8) the curvature of mobile dislocations in constrained volumes (Dunstan & Bushby, 2014; Li et al., 2016).

We can rule out some of the models listed above for application to olivine based on our experimental observations. We observe a yield stress that is temperature and grain size dependent. Some models focus on long-range stress fields or dislocation curvature (models listed under 7 and 8, respectively), which will not be temperature dependent. Several models listed above only result in a grain size dependence once some macroscopic plastic strain has accumulated (models listed under 5 and 6), which implies that the yield stress itself is not necessarily grain size dependent. Models listed under 1, 3, and 4 do require some plastic strain before grain size effects are realized, but that initial plastic strain can be localized enough that it is not detectable prior to macroscopic yielding (e.g., Maaß & Derlet, 2018). Therefore, models listed under 1–4 are all potentially applicable as they result in a grain size-dependent yield stress and involve local interactions leading to a temperature dependence (although long-range interactions can also arise in models involving

GNDs). The model of Li (1963) and Bata and Pereloma (2004) are particularly interesting because they involve the nucleation of dislocations at grain boundaries. Recent nanoindentation experiments using spherical indenters (Kumamoto et al., 2017) and transmission electron microscopy of deformed olivine aggregates (Thieme et al., 2018) suggest that grain and subgrain boundaries are dislocation sources in olivine.

The remaining models (items 1 through 4 in the list above) all result in the same basic form of constitutive equation,

$$\sum = \sigma_{\mathrm{L}} + \ Kd^{-\frac{1}{2}} \ , \tag{12}$$

where σ_{L} is the intrinsic resistance of the lattice to dislocation motion (i.e., the lattice friction) and K is a material-dependent constant whose derivation varies from model to model. The right-hand side of this equation is generally referred to as the Hall-Petch relationship, and here we set it equal to the local resistance to dislocation motion, Σ, because of the observed temperature dependence of yield. A similar approach was taken by Renner et al. (2002) to describe the deformation of calcite.

4.3. Strain Hardening

All of the samples deformed in the present study exhibit some degree of strain hardening. Strain hardening in crystalline materials is typically interpreted to result from increases in dislocation density that progressively limit the velocity of mobile dislocations. Dislocations that interact to form locked structures (e.g., dipoles or junctions) can preserve the dislocation arrangement after the sample is macroscopically unloaded. Thus, if the sample is reloaded, the hardened state of the sample is preserved, and the sample will not yield until the stress obtained just before unloading is reached. If the unloaded sample is reloaded in the reverse direction (e.g., to negative differential stress), then yield will not occur until the stress in the reverse direction is the same magnitude as the stress in the forward direction prior to unloading, hence the term *isotropic hardening*. In contrast, accumulations of GNDs can generate a significant long-range stress field that acts as a back stress for mobile dislocations, and therefore, yield in the reverse direction can occur at a lower applied stress than the initial yield stress. This phenomenon is often referred to as the Bauschinger effect (Bauschinger, 1886) and the associated hardening as *kinematic hardening*. The cyclical loading experiments presented here exhibit a significant Bauschinger effect (Figure 7). In subsequent cycles, the yield stresses are similar but reduced relative to the yield stress in the initial cycle. The reduction in the yield stress occurs because in each new cycle there is a residual back stress from the previous cycle that now acts in the same direction as the applied stress. Thus, the yield stress in each new cycle corresponds to the inherent yield strength minus the previously accumulated back stress. Further deformation acts to relax the back stress, which effectively results in strain hardening. Once all of the back stress is relaxed, a back stress of opposite sign begins to accumulate, opposing the applied stress, which is manifested as continued hardening until a maximum in the back stress is reached. Therefore, following the analysis of Kuhlmann-Wilsdorf and Laird (1979), we estimate the magnitude of the associated back stress by taking half the difference between the flow stress and the yield stress for cycles after the initial cycle. The values of the estimated back stress presented in Table 2 range from 1.1 to 2.6 GPa.

The maximum flow stresses and back stresses measured in cyclical experiments are presented in Figure 9 as a function of temperature. Although not well resolved, we do not observe a measurable temperature dependence of the back stress, consistent with the temperature independence evident in equation (11). In contrast, the maximum flow stress is demonstrably temperature dependent, and that temperature dependence is consistent with the temperature dependence of the yield stress. Since the total magnitude of hardening during the first loading cycle (i.e., flow stress minus yield stress) is on the order of the apparent back stress (Table 2), it is reasonable to assume that the hardening observed in our experiments is dominated by kinematic, rather than isotropic, hardening. The importance of kinematic hardening in moderating the strength of olivine is also evidenced by the nanoindentation experiments of Kumamoto et al. (2017) that revealed significant accumulation of GNDs and residual stresses associated with low-temperature plasticity.

Although we can infer that kinematic hardening is dominant, the best available model to describe the evolution of hardening is not clear. A rigorous treatment based on the accumulation and interaction of dislocations as well as the partitioning of those interactions into isotropic and kinematic components requires

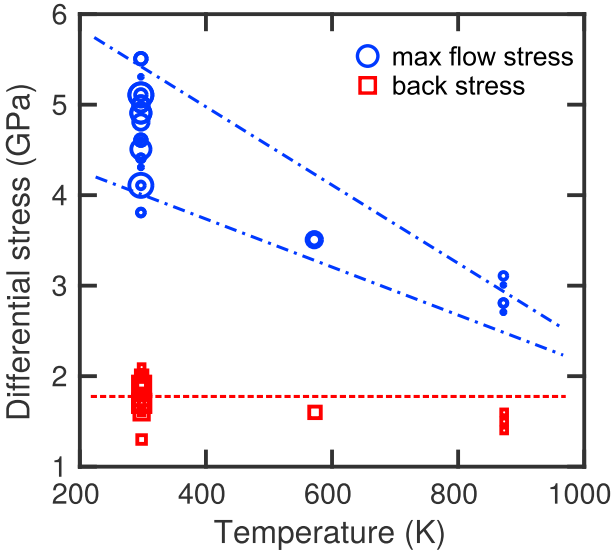

Figure 9. Maximum flow stress and back stress as a function of temperature, measured during cyclical-loading experiments. The size of the marker indicates the cycle from which the data are taken, with small markers indicating early cycles and large markers indicating late cycles. The red dashed line corresponds to the back stress calculated from the calibrated model discussed in section 4.4. The blue dot-dashed lines delimit the maximum flow stress predicted by the same model for the range of grain sizes explored in this study.

understanding of the spatial distribution and anisotropy of dislocation density (Evers et al., 2004b) and is beyond the scope of the present work. Many popular models simplify the problem greatly by treating dislocation density as a zero-dimensional scalar and evaluating the evolution of dislocation density as a competition between the recovery rate and storage rate of dislocations, with key examples given by Mecking and Kocks (1981) and Bammann (1984). The competition between these processes leads to a saturation in dislocation density and, therefore, to a steady state stress, similar to our observations.

To employ these models in a physically based manner relies on knowledge of dislocation storage and recovery mechanisms. Treatment of storage mechanisms is complicated by the fact that dislocation arrays, subgrain boundaries, and grain boundaries can all act as storage sites (e.g., Sinclair et al., 2006). Treatments of recovery also vary substantially. Most parameterizations of recovery in metals assume that cross slip is the dominant recovery mechanism, but cross slip in olivine appears to only be important at temperatures above 600 °C (Phakey et al., 1972; Poirier, 1976). Dislocation climb is another possible recovery mechanism, which can occur by static, diffusion-limited climb at high temperatures (e.g., Weertman, 1957). Gouriet et al. (2017) explored the role of this mechanism in olivine using discrete-dislocation dynamics, resulting in steady state flow. As an alternative, Nes (1997) pointed out that dynamic, stress-enhanced climb with only short-range diffusion is a potential process for controlling recovery rates at low temperatures. Our results suggest that the back stress appears to reach a steady state value, and although not well resolved, that value appears to be temperature independent, which would not be the case if any type of climb were the limiting mechanism. Identifying the mechanisms of dislocation recovery in olivine at low temperatures is a clear target for future investigation.

Additional difficulty in modeling dislocation density arises when considering the deformation of polycrystalline aggregates. Accumulation of dislocations at grain boundaries likely depends on the ability of grain boundaries to nucleate dislocations or transmit dislocations to neighboring grains (e.g., Evers et al., 2004a; Hirth, 1972). The long-range stress fields associated with the accumulation of dislocations near grain boundaries may also screen the stress fields of dislocations in neighboring grains, effectively reducing back stresses (Sinclair et al., 2006).

Furthermore, even if a robust formulation of the evolution of dislocation density is derived, calculating the effective back stress as a result of those dislocations is nontrivial. As reviewed by Bayley et al. (2006), the stress state associated with GND fields depends on the gradients in dislocation density, and therefore the spatial distribution of GNDs must be tracked.

Given the complications and uncertainties associated with modeling the evolution of dislocation density and back stress, we opt for a simple empirical parameterization of strain hardening that can still explain our data. We do not consider the underlying GND density and instead directly estimate the evolution of the back stress according to the relation

$$\frac{d\sigma_b}{d\varepsilon_p} = \gamma\left[\sigma_{b,\max} - \mathrm{sgn}\left(\dot{\varepsilon}_p\right)\sigma_b\right] \quad , \tag{13}$$

where ε_p is the plastic strain, $\sigma_{b,max}$ is the maximum back stress, $\dot{\varepsilon}_p$ is the plastic strain rate, and γ is a rate constant. This equation results in a back stress that gradually approaches $\sigma_{b,max}$ at a rate determined by γ. For unidirectional loading, a simple analytical solution exists for σ_b (ε_p). Although formatted differently, equation (13) is equivalent to the popular formulation of Armstrong and Frederick (1966), in which they consider the balance between a hardening rate and a dynamic recovery rate, analogous to the balance of dislocation storage and recovery. In the nomenclature of the Armstrong and Frederick model, $\gamma\sigma_{b,max}$ is the initial hardening modulus.

Table 3
Best Fit Model Parameters for Equations (11), (12), and (13)

A (s^{-1})	ΔF (kJ/mol)	σ_L (GPa)	K (GPa $\mu m^{0.5}$)	γ	$\sigma_{b,max}$ (GPa)
$10^{20.7 \pm 1.2}$	550 ± 90	3.1 ± 0.4	3.2 ± 0.4	75 ± 20	1.8 ± 0.2

An interesting implication arises from the above discussion of strain hardening in olivine. All the hardening is assumed to come from the generation of a back stress, which is theoretically independent of temperature. On initial loading, the flow stress is simply the sum of the yield stress and the back stress, and because the yield stress is temperature dependent, the flow stress will also be temperature dependent, as evidenced by Figure 9. However, the *magnitude* of strain hardening in olivine (the increase in stress between the yield stress and flow stress), if due entirely to back stresses, will not be temperature dependent. These considerations imply that roughly 2 GPa of hardening will occur regardless of the temperature or strain rate, as described by the right-hand side of equation (1). That said, at sufficiently high temperatures, when temperature-dependent recovery mechanisms such as dislocation climb contribute significantly, we may expect the magnitude of hardening to become temperature dependent. We suggest this transition in dominant recovery mechanism effectively demarcates the rheological transition between exponential creep (i.e., low-temperature plasticity) and power law creep (i.e., dislocation creep or dislocation-accommodated grain boundary sliding).

There are similar implications for the role of pressure in affecting the strength of olivine. The structure of dislocation cores is expected to be a function of the hydrostatic component of the stress, which then modifies the lattice friction, σ_L (Amodeo et al., 2012; Cordier et al., 2012). Thus, changing the pressure only modifies the first term on the right-hand side of equation (11), and therefore, like temperature, only modifies the yield stress. The long-range interactions associated with the back stress should be independent of pressure (aside from the small effect of pressure on the elastic moduli), and we therefore hypothesize that the magnitude of strain hardening is independent of pressure.

4.4. Flow Law Calibration

We calibrate a constitutive model for low-temperature plasticity of olivine aggregates based on equations (11), (12), and (13). For calibration, we use the yield stresses and flow stresses from all experiments. Our data set is not particularly sensitive to variations in temperature, so we incorporate in our fitting procedure other data sets for which stress, temperature, strain rate, and grain size are available (Long et al., 2011; Mei et al., 2010). We also only use data from experiments conducted at $T \leq 1073$ K to remove experiments in which high-temperature creep processes may have contributed significantly to the measured mechanical response. Note that we do not use the data set from Demouchy et al. (2013) because their yield stresses were picked at an arbitrarily set value of the total strain (1%), necessitated by the lack of an obvious yield point in their mechanical data. Best fit values for all parameters aside from γ were obtained using a nonlinear optimization routine in the MATLAB® optimization toolbox to minimize the misfit between measured and predicted stresses. The value of γ was determined in a separate fitting procedure using the full stress-strain curves from cyclical experiments. Values for the best fit parameters are presented in Table 3. Errors in parameter values were determined using a bootstrapping procedure in which subsets of the data were randomly chosen and a set of best fit values were obtained for each subset. Reported errors are the standard deviation of the distributions of best fit values.

The calibrated model is compared to data in Figures 8 and 10. Figure 8 presents all of the data collected at room temperature and flow laws from previous studies extrapolated to room temperature. The grain size dependence is evident in both the model and the data, and the curvature of the model suggests that most of our data lie at grain sizes within the transition between grain size-independent and grain size-dependent deformation. Figure 10 presents our data and a selection of previously published data as a function of temperature, including data from low-strain measurements representing initial yield (Figure 10a), data collected at large strains (Figure 10b), and a normalization of the full data set to large grain size and no plastic strain using our calibrated model. The grain size dependence is clear in the low-strain data (Figure 10a), with good correspondence to the model. The model curves also reveal a prediction that the temperature dependence of yield is a function of grain size. At high strain (Figure 10b), the model still predicts a moderate grain size

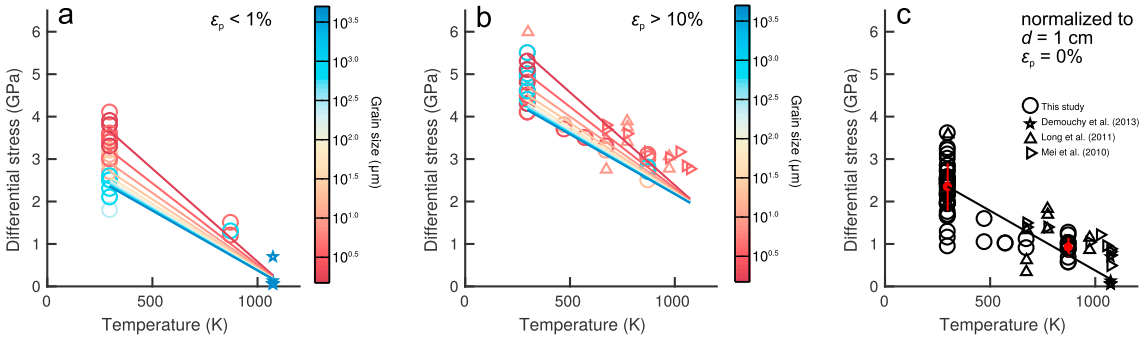

Figure 10. Comparison of stresses predicted by our calibrated model to data from this and previous studies as a function of temperature. Data and model are presented for (a) yield, (b) high strain, and (c) normalized to large grain size and zero plastic strain. In (a) and (b), model curves and data points are colored by grain size. In (c), means and standard deviations of large groups of data at 273 and 873 K are represented by a red circle and vertical line.

dependence, but this dependence is less evident in the data. The normalized data set reveals a general temperature dependence consistent with the model and demonstrates that stresses are predicted to within ~30% (Figure 10c).

Several aspects of the best fit parameter values are noteworthy in comparison to previous results. The activation energy of 550 kJ/mol is within the range of previously determined activation energies of 566 (Idrissi et al., 2016), 564 (Raterron et al., 2004), 498 (B. Evans & Goetze, 1979), 458 (Long et al., 2011), 450 (Demouchy et al., 2013), and 320 (Mei et al., 2010). The value for the lattice friction (i.e., the Peierls stress) of 3.1 ± 0.4 GPa determined here is at the low end of the range of previous estimates. The highest published estimates of the lattice friction in olivine are ~15 GPa (Demouchy et al., 2013; Raterron et al., 2004). The lowest published estimate of 3.8 ± 0.7 GPa from Idrissi et al. (2016) is within error of our result, and interestingly, Idrissi et al. obtained this estimate of σ_L through direct observation of dislocation velocities and incorporation of those velocities into a discrete dislocation dynamics simulation. That approach avoids any grain boundary effects and therefore is likely the only estimate of olivine strength in the literature that is not subject to size effects. Thus, it is encouraging that we obtain a similar value of lattice friction after accounting for size effects through equation (12).

The ability of the model to predict strain hardening and other behavior during cyclical experiments is explored in Figure 11. The model is specifically compared to experiment San388, which involved loading cycles at three different temperatures. The model encouragingly captures the magnitude and rate of hardening at each temperature. It also captures the Bauschinger effect, which is revealed by the essentially constant yield stress between the first forward and the second forward loading path, even though the temperature was decreased before the second forward loading path.

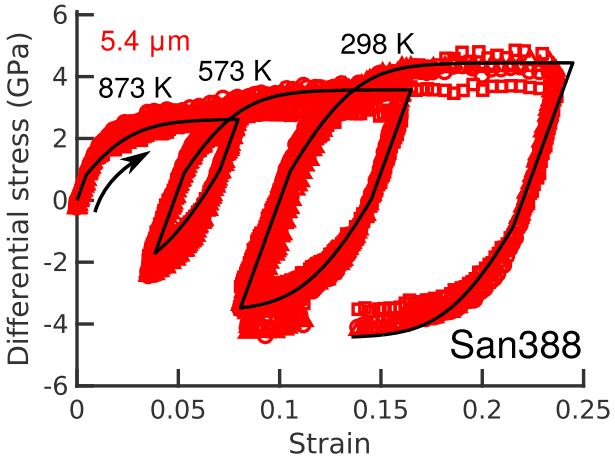

Figure 11. Comparison of the calibrated model (black line) to mechanical data from a cyclical loading experiment (red markers). Each of the three cycles was conducted at a separate temperature as noted. The different red marker shapes are as in Figure 7.

4.5. Application to the Lithosphere

The model calibrated in the previous section has several major implications for the strength of the lithosphere. First, as initially suggested by Kumamoto et al. (2017), the grain size dependence of yield strength in olivine suggests that the strength of the coarse-grained upper mantle may be lower by a factor of 5 than previous predictions based on experiments on fine-grained olivine aggregates. However, the high degree of strain hardening observed in our experiments implies that, although the lithosphere may be initially weak at yield, it will strengthen quickly with progressive deformation.

We explore these effects in Figure 12 through an extrapolation of our model to oceanic lithosphere. We assume a temperature profile for 80-myr-old crust and calculate the strength of plastically deforming olivine over a range of strain. Strength profiles are constructed following

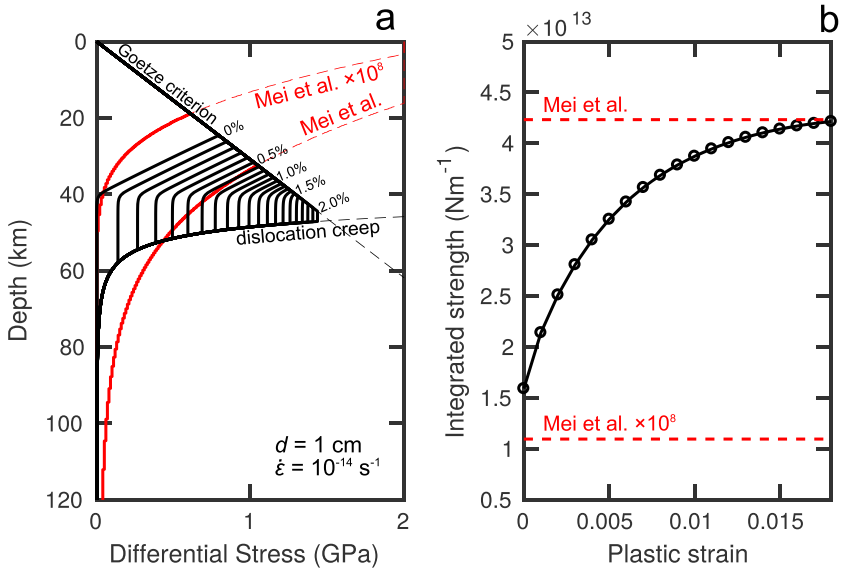

Figure 12. Estimates of lithospheric strength from the constitutive model calibrated in this study. (a) Strength profiles calculated for a constant strain rate and temperature profile relevant for oceanic lithosphere. The temperature profile was calculated for a mantle potential temperature of 1300 °C and 80-myr-old crust (Turcotte & Schubert, 2014, pp. 185–187). Black curves are stresses predicted for low-temperature plasticity at a variety of plastic strains (labeled by percent). These curves are bounded by the Goetze criterion, indicating the onset of brittle mechanisms, and high-temperature dislocation creep for dry olivine (G. Hirth & Kohlstedt, 2003). Red curves represent the flow law from Mei et al. (2010) and the same flow law as modified to fit flexural data at Hawaii by Zhong and Watts (2013), referred to as "Mei et al. $\times 10^8$." (b) Integrated strength of the lithosphere calculated for the strength profiles in (a) as a function of strain. Circles correspond to the individual profiles depicted in (a).

Kohlstedt et al. (1995), but for simplicity, we neglect the crustal contribution and do not use a frictional failure envelope to constrain the brittle regime. We use the Goetze criterion (Briegel & Goetze, 1978; Evans et al., 1990; Kohlstedt et al., 1995) as a marker of the onset of brittle deformation to bound the shallow end of the curves describing olivine plasticity. We bound the deep end of these curves with a flow law for dry, high-temperature dislocation creep of olivine (G. Hirth & Kohlstedt, 2003), which follows from our suggestion above that the intersection of the curves for high-temperature creep and low-temperature plasticity potentially marks the point at which diffusion-limited recovery processes begin to compete significantly with the hardening processes. We numerically integrate these curves to calculate the integrated strength of the oceanic lithosphere as a function of strain (Figure 12b).

The calculation presented in Figure 12 illustrates our model prediction that the lithosphere is initially weak but strengthens quickly with progressive strain. At 0% plastic strain, the plastic strength is depth dependent, reflecting the temperature dependence of yield, and decreases to 0 strength at ~40-km depth. With increasing strain, this curve representing our model for low-temperature plasticity is shifted uniformly to higher stresses due to temperature-independent hardening. Importantly, the depth at which brittle processes begin to operate becomes increasingly deeper with progressive plastic strain. In contrast, the depth at which high-temperature creep begins to control the strength becomes increasingly shallower. Thus, with increasing plastic strain, we predict that low-temperature plasticity operates over a decreasing depth range that vanishes after ~2% strain for the conditions of 80-myr-old oceanic lithosphere presented in Figure 12. This model correspondingly predicts that the integrated strength (Figure 12b) reaches a steady state value after the same amount of strain.

The strain dependence of lithospheric strength may explain unreconciled geophysical observations of the strength of the oceanic lithosphere. Zhong and Watts (2013) modeled the flexural response around the Hawaiian islands using a viscoelastic model incorporating the low-temperature plasticity flow law of Mei et al. (2010). They found that the preexponential constant, analogous to A in our equation (10), needed to be increased by a factor of 10^8 for the modeling to appropriately reproduce the flexure data. This result was corroborated by Hunter and Watts (2016), who analyzed the same region with yield-strength

envelopes constructed from a variety of laboratory-derived flow laws. However, Hunter and Watts (2016) also modeled the flexure of oceanic lithosphere entering circum-Pacific subduction zones and found that the flow law of Mei et al. (2010) did sufficiently reproduce the observations. A potential explanation of this discrepancy is that the flexure associated with the volcanic loads of the Hawaiian archipelago only produces relatively small strains, and therefore, the lithospheric mantle does not undergo much strain hardening. In contrast, it seems possible that relatively higher strains would be encountered during flexure at Pacific trenches, such that the lithosphere in these regions would be subject to significant strain hardening. Therefore, in Figure 12, we compare the flow law of Mei et al. (2010) and its modification by Zhong and Watts (2013) to our own model. As hypothesized, our prediction of the integrated lithospheric strength at yield is consistent with the weaker flow law and therefore with the observations in Hawaii, whereas our prediction of integrated strength at high strain is consistent with the stronger flow law and therefore with the observations at trenches. Thus, variable estimates of lithospheric strength from geophysical data may actually be consistent with each other if the magnitude of plastic strain is taken into account.

5. Conclusions

The strength of Earth's lithosphere is ultimately dependent on the microphysical mechanisms of plastic deformation in olivine. A wide variety of experimental studies of the plasticity of olivine have previously been conducted, with relatively little agreement among the results. We identify grain size and the magnitude of plastic strain as key parameters that vary widely among previous experiments and therefore complicate comparison among different data sets and extrapolation to geological conditions.

Based on these results, we developed and calibrated a new constitutive model for low-temperature plasticity in olivine that accounts for grain size effects and strain magnitude, using physical arguments based on local and long-range interactions of lattice dislocations. The key features of our observations and model are as follows: (1) Fine-grained samples have a higher yield stress than coarse-grained samples; (2) significant strain hardening occurs leading to a nearly constant flow stress; (3) the yield stress and maximum flow stress both decrease with increasing temperature; and (4) the magnitude of hardening, and therefore the magnitude of the effective back stress resulting from dislocation interactions, is independent of both grain size and temperature, at least within the resolution of our data set.

Our calibrated model has several implications for the strength of Earth's lithosphere. First, we predict that the relatively coarse-grained upper mantle has a much lower yield strength (approximately by a factor of 5) than the yield strength measured in most previous experiments on fine-grained olivine aggregates. This prediction is consistent with the analyses of flexure of apparently weak oceanic lithosphere near Hawaii (Zhong & Watts, 2013). Second, we predict the strength of the lithosphere to be strongly dependent on strain over the first 2% of strain, and the flexural response of apparently strong oceanic lithosphere near Pacific trenches may be a manifestation of high strains associated with high plate curvature. Strain hardening in Earth, however, is likely limited by the onset of diffusion-based recovery mechanisms typically associated with dislocation creep, which will be more effective at higher temperatures in the deeper interior.

Acknowledgments
We are grateful for the efficient and excellent technical assistance of Haiyan Chen at beamline 6-BM-B at the Advanced Photon Source. We are also thankful for help with sample and assembly preparation from Rellie Goddard and fabrication of assembly parts by Kurt Leinenweber, Jamie Long, and James King. The manuscript was greatly improved by thoughtful reviews from Joerg Renner and Claudia Trepmann. This research was supported by Natural Environment Research Council grant NE/M000966/1 to L. N. H. and D. W.; Advanced Photon Source General User Proposal 55176 to L. N. H., D. L. K., D. L. G., and W. B. D.; National Science Foundation Award EAR-1361319 to W. B. D. and EAR-1806791 to K. M. K.; and the Department of Energy National Nuclear Security Administration Stewardship Science Graduate Fellowship to C. D. M. Use of the COMPRES Cell Assembly Project was supported by COMPRES under NSF Cooperative Agreement EAR 1661511. The data used are presented in the figures and tables.

References

Abramson, E. H., Brown, J. M., Slutsky, L. J., & Zaug, J. (1997). The elastic constants of San Carlos olivine to 17 GPa. *Journal of Geophysical Research*, Geophys. Monogr. Ser., *102*(B6), 12,253–12,263. https://doi.org/10.1029/97JB00682

Amodeo, J., Carrez, P., & Cordier, P. (2012). Modelling the effect of pressure on the critical shear stress of MgO single crystals. *Philosophical Magazine*, *92*(12), 1523–1541. https://doi.org/10.1080/14786435.2011.652689

Armstrong, Peter J., & Frederick, C. O. (1966). A mathematical representation of the multiaxial Bauschinger effect.

Armstrong, R., Codd, I., Douthwaite, R. M., & Petch, N. J. (1962). The plastic deformation of polycrystalline aggregates. *The Philosophical Magazine: A Journal of Theoretical Experimental and Applied Physics*, *7*(73), 45–58. https://doi.org/10.1080/14786436208201857

Ashby, M. F. (1970). The deformation of plastically non-homogeneous materials. *Philosophical Magazine*, *21*(170), 399–424. https://doi.org/10.1080/14786437008238426

Bai, Q., Mackwell, S. J., & Kohlstedt, D. L. (1991). High-temperature creep of olivine single crystals 1. Mechanical results for buffered samples. *Journal of Geophysical Research*, *96*(B2), 2441–2463. https://doi.org/10.1029/90JB01723

Bammann, D. J. (1984). An internal variable model of viscoplasticity. *International Journal of Engineering Science*, *22*(8-10), 1041–1053. https://doi.org/10.1016/0020-7225(84)90105-8

Bata, V., & Pereloma, E. V. (2004). An alternative physical explanation of the Hall–Petch relation. *Acta Materialia*, *52*(3), 657–665. https://doi.org/10.1016/j.actamat.2003.10.002

Bauschinger, J. (1886). "Ueber die Veranderung der elasticitatsgrenge und der festigkeit des eisens und stahls durch strecken und quetschn, durch erwarmen und abkuhlen und durch oftmal wiederholte beanspruchung." Mitteilungen Aus Dem Mechanisch-Technischen Laboratorium Der K. Technischen Hochschule in Munchen 13. https://ci.nii.ac.jp/naid/10010131844/

Bayley, C. J., Brekelmans, W. A. M., & Geers, M. G. D. (2006). A comparison of dislocation induced back stress formulations in strain gradient crystal plasticity. *International Journal of Solids and Structures*, *43*(24), 7268–7286. https://doi.org/10.1016/j.ijsolstr.2006.05.011

Boettcher, M. S., Hirth, G., & Evans, B. (2007). Olivine friction at the base of oceanic seismogenic zones. *Journal of Geophysical Research*, *112*, B01205. https://doi.org/10.1029/2006JB004301

Brace, W. F., & Kohlstedt, D. L. (1980). Limits on lithospheric stress imposed by laboratory experiments. *Journal of Geophysical Research*, *85*(B11), 6248–6252. https://doi.org/10.1029/JB085iB11p06248

Briegel, U., & Goetze, C. (1978). Estimates of differential stress recorded in the dislocation structure of Lochseiten limestone (Switzerland). *Tectonophysics*, *48*(1-2), 61–76. https://doi.org/10.1016/0040-1951(78)90086-0

Buffett, B. A., & Becker, T. W. (2012). Bending stress and dissipation in subducted lithosphere. *Journal of Geophysical Research*, *117*, B05413. https://doi.org/10.1029/2012JB009205

Conrad, H. (1963). Effect of grain size on the lower yield and flow stress of iron and steel. *Acta Metallurgica*, *11*(1), 75–77. https://doi.org/10.1016/0001-6160(63)90134-2

Conrad, H., Feuerstein, S., & Rice, L. (1967). Effects of grain size on the dislocation density and flow stress of niobium. *International Journal of Green Nanotechnology: Materials Science and Engineering*, *2*(3), 157–168.

Cordero, Z. C., Knight, B. E., & Schuh, C. A. (2016). Six decades of the Hall–Petch effect—A survey of grain-size strengthening studies on pure metals. *International Materials Reviews*, *61*(8), 495–512. https://doi.org/10.1080/09506608.2016.1191808

Cordier, P., Amodeo, J., & Carrez, P. (2012). Modelling the rheology of MgO under Earth's mantle pressure, temperature and strain rates. *Nature*, *481*(7380), 177–180. https://doi.org/10.1038/nature10687

Cottrell, A. H. (1953). Theory of dislocations. *Progress in Physics of Metals/Uspehi Fiziki Metallov*, *4*, 205–264.

Demouchy, S., Tommasi, A., Ballaran, T. B., & Cordier, P. (2013). Low strength of Earth's uppermost mantle inferred from tri-axial deformation experiments on dry olivine crystals. *Physics of the Earth and Planetary Interiors*, *220*(July), 37–49. https://doi.org/10.1016/j.pepi.2013.04.008

Dixon, N. A., & Durham, W. B. (2018). Measurement of activation volume for creep of dry olivine at upper-mantle conditions. *Journal of Geophysical Research: Solid Earth*, *123*, 8459–8473. https://doi.org/10.1029/2018JB015853

Druiventak, A., Trepmann, C. A., Renner, J., & Hanke, K. (2011). Low-temperature plasticity of olivine during high stress deformation of peridotite at lithospheric conditions—An experimental study. *Earth and Planetary Science Letters*, *311*(3–4), 199–211. https://doi.org/10.1016/j.epsl.2011.09.022

Dunstan, D. J., & Bushby, A. J. (2014). Grain size dependence of the strength of metals: The Hall–Petch effect does not scale as the inverse square root of grain size. *International Journal of Plasticity*, *53*(February), 56–65. https://doi.org/10.1016/j.ijplas.2013.07.004

Durham, W. B., & Goetze, C. (1977). Plastic flow of oriented single crystals of olivine: 1. Mechanical data. *Journal of Geophysical Research*, *82*(36), 5737–5753. https://doi.org/10.1029/JB082i036p05737

Durham, W. B., Mei, S., Kohlstedt, D. L., Wang, L., & Dixon, N. A. (2009). New measurements of activation volume in olivine under anhydrous conditions. *Physics of the Earth and Planetary Interiors*, *172*(1-2), 67–73. https://doi.org/10.1016/j.pepi.2008.07.045

England, P., & Molnar, P. (2015). Rheology of the lithosphere beneath the central and western Tien Shan. *Journal of Geophysical Research: Solid Earth*, *120*, 3803–3823. https://doi.org/10.1002/2014JB011733

Evans, A. G., & Rawlings, R. D. (1969). The thermally activated deformation of crystalline materials. *Physica Status Solidi*, *34*(1), 9–31. https://doi.org/10.1002/pssb.19690340102

Evans, B., Fredrich, J. T., & Wong, T.-F. (1990). The brittle-ductile transition in rocks: Recent experimental and theoretical progress. In *Geophysical Monograph Series* (pp. 1–20). Washington, DC: American Geophysical Union.

Evans, B., & Goetze, C. (1979). The temperature variation of hardness of olivine and its implication for polycrystalline yield stress. *Journal of Geophysical Research*, *84*(B10), 5505–5524. https://doi.org/10.1029/JB084iB10p05505

Evers, L. P., Brekelmans, W. A. M., & Geers, M. G. D. (2004a). Scale dependent crystal plasticity framework with dislocation density and grain boundary effects. *International Journal of Solids and Structures*, *41*(18–19), 5209–5230. https://doi.org/10.1016/j.ijsolstr.2004.04.021

Evers, L. P., Brekelmans, W. A. M., & Geers, M. G. D. (2004b). Non-local crystal plasticity model with intrinsic SSD and GND effects. *Journal of the Mechanics and Physics of Solids*, *52*(10), 2379–2401. https://doi.org/10.1016/j.jmps.2004.03.007

Faul, U. H., Fitz Gerald, J. D., Farla, R. J. M., Ahlefeldt, R., & Jackson, I. (2011). Dislocation creep of fine-grained olivine. *Journal of Geophysical Research*, *116*, B01203. https://doi.org/10.1029/2009JB007174

Frost, H. J., & Ashby, M. F. (1982). *Deformation mechanism maps: The plasticity and creep of metals and ceramics*. Oxford, UK: Pergamon Press.

Garofalo, F. (1963). An empirical relation defining the stress dependence of minimum creep rate in metals. *Transactions of AIME*, *227*, 351–356.

Gouriet, K., Cordier, P., Boioli, F., Demouchy, S. A., Tommasi, A., & Devincre, B. (2017). "A unified creep law to define the rheology of olivine in the lithospheric mantle." AGU Fall Meeting Abstracts. http://adsabs.harvard.edu/abs/2017AGUFMDI22A.07G.

Hall, E. O. (1951). The deformation and ageing of mild steel: III Discussion of results. *Proceedings of the Physical Society. Section B*, *64*(9), 747–753. https://doi.org/10.1088/0370-1301/64/9/303

Hansen, L. N., Zimmerman, M. E., & Kohlstedt, D. L. (2011). Grain boundary sliding in San Carlos olivine: Flow law parameters and crystallographic-preferred orientation. *Journal of Geophysical Research*, *116*, B08201. https://doi.org/10.1029/2011JB008220

Harder, J. (1999). A crystallographic model for the study of local deformation processes in polycrystals. *International Journal of Plasticity*, *15*(6), 605–624. https://doi.org/10.1016/S0749-6419(99)00002-9

Hirth, G., & Kohlstedt, D. (2003). Rheology of the upper mantle and the mantle wedge: A view from the experimentalists. In J. Eiler (Ed.), *Geophysical Monograph Series* (Vol. 138, pp. 83–105). Washington, DC: American Geophysical Union.

Hirth, G., & Kohlstedt, D. L. (1995). Experimental constraints on the dynamics of the partially molten upper mantle: 2. Deformation in the dislocation creep regime. *Journal of Geophysical Research*, *100*(B8), 15,441–15,449. https://doi.org/10.1029/95JB01292

Hirth, J. P. (1972). The influence of grain boundaries on mechanical properties. *Metallurgical Transactions*, *3*(12), 3047–3067. https://doi.org/10.1007/BF02661312

Hou, X. D., Bushby, A. J., & Jennett, N. M. (2008). Study of the interaction between the indentation size effect and Hall–Petch effect with spherical indenters on annealed polycrystalline copper. *Journal of Physics D: Applied Physics*, *41*(7), 074006. https://doi.org/10.1088/0022-3727/41/7/074006

Hunter, J., & Watts, A. B. (2016). Gravity anomalies, flexure and mantle rheology seaward of circum-pacific trenches. *Geophysical Journal International*, *207*(1), 288–316. https://doi.org/10.1093/gji/ggw275

Idrissi, H., Bollinger, C., Boioli, F., Schryvers, D., & Cordier, P. (2016). Low-temperature plasticity of olivine revisited with in Situ TEM nanomechanical testing. *Science Advances*, *2*(3), e1501671. https://doi.org/10.1126/sciadv.1501671

Isaak, D. G. (1992). High-temperature elasticity of iron-bearing olivines. *Journal of Geophysical Research*, *97*(B2), 1871–1885. https://doi.org/10.1029/91JB02675

Jain, C., Korenaga, J., & Karato, S.-I. (2017). On the yield strength of oceanic lithosphere. *Geophysical Research Letters*, *44*, 9716–9722. https://doi.org/10.1002/2017GL075043

Karato, S.-I., Rubie, D. C., & Yan, H. (1993). Dislocation recovery in olivine under deep upper mantle conditions: Implications for creep and diffusion. *Journal of Geophysical Research*, *98*(B6), 9761–9768. https://doi.org/10.1029/93JB00472

Kocks, U. F., Argon, A. S., & Ashby, M. F. (1975). Thermodynamics and kinetics of slip. *Progress in Materials Science*, *19*, 1–281.

Kohlstedt, D. L., Evans, B., & Mackwell, S. J. (1995). Strength of the lithosphere: Constraints imposed by laboratory experiments. *Journal of Geophysical Research*, *100*(B9), 17,587–17,602. https://doi.org/10.1029/95JB01460

Kohlstedt, D. L., & Hansen, L. N. (2015). 2.18—Constitutive equations, rheological behavior, and viscosity of rocks. In G. Schubert (Ed.), *Treatise on geophysics (second edition)* (pp. 441–472). Oxford: Elsevier. https://doi.org/10.1016/B978-0-444-53802-4.00042-7

Kranjc, K., Rouse, Z., Flores, K. M., & Skemer, P. (2016). Low-temperature plastic rheology of olivine determined by nanoindentation. *Geophysical Research Letters*, *43*, 176–184. https://doi.org/10.1002/2015GL065837

Kuhlmann-Wilsdorf, D., & Laird, C. (1979). Dislocation behavior in fatigue II. Friction stress and back stress as inferred from an analysis of hysteresis loops. *International Journal of Green Nanotechnology: Materials Science and Engineering*, *37*(2), 111–120.

Kumamoto, K. M., Thom, C. A., Wallis, D., Hansen, L. N., Armstrong, D. E. J., Warren, J. M., et al. (2017). Size effects resolve discrepancies in 40 years of work on low-temperature plasticity in olivine. *Science Advances*, *3*(9), e1701338. https://doi.org/10.1126/sciadv.1701338

Kumazawa, M., & Anderson, O. L. (1969). Elastic moduli, pressure derivatives, and temperature derivatives of single-crystal olivine and single-crystal forsterite. *Journal of Geophysical Research*, *74*(25), 5961–5972. https://doi.org/10.1029/JB074i025p05961

Li, J. (1963). Petch relation and grain boundary sources. *Transactions of the Metallurgical Society of AIME*, *227*(1), 239.

Li, Y., Bushby, A. J., & Dunstan, D. J. (2016). The Hall-Petch effect as a manifestation of the general size effect. *Proceedingsof the Mathematical, Physical, and Engineering Sciences/the Royal Society*, *472*(2190), 20150890. https://doi.org/10.1098/rspa.2015.0890

Long, H., Weidner, D. J., Li, J. C., & Wang, L. (2011). Deformation of olivine at subduction zone conditions determined from in situ measurements with synchrotron radiation. *Physics of the Earth and Planetary Interiors*, *186*(1–2), 23–35. https://doi.org/10.1016/j.pepi.2011.02.006

Maaß, R., & Derlet, P. M. (2018). Micro-plasticity and recent insights from intermittent and small-scale plasticity. *Acta Materialia*, *143*, 338–363. https://doi.org/10.1016/j.actamat.2017.06.023

Matysiak, A. K., & Trepmann, C. A. (2012). Crystal–plastic deformation and recrystallization of peridotite controlled by the seismic cycle. *Tectonophysics*, *530–531*(March), 111–127.

Mecking, H., & Kocks, U. F. (1981). Kinetics of flow and strain-hardening. *Acta Metallurgica*, *29*(11), 1865–1875. https://doi.org/10.1016/0001-6160(81)90112-7

Mei, S., Suzuki, A. M., Kohlstedt, D. L., Dixon, N. A., & Durham, W. B. (2010). Experimental constraints on the strength of the lithospheric mantle. *Journal of Geophysical Research*, *115*, B08204. https://doi.org/10.1029/2009JB006873

Meyers, M. A., & Ashworth, E. (1982). A model for the effect of grain size on the yield stress of metals. *Philosophical Magazine A*, *46*(5), 737–759. https://doi.org/10.1080/01418618208236928

Nes, E. (1997). Modelling of work hardening and stress saturation in FCC metals. *Progress in Materials Science*, *41*(3), 129–193. https://doi.org/10.1016/S0079-6425(97)00032-7

O'Haver, T. C. (2018). Pragmatic introduction to signal processing 2019: Applications in scientific measurement. Independently published.

Paterson, M. S. (1990). Rock deformation experimentation. In *The brittle-ductile transition in rocks*, (pp. 187–194). Washington, DC: American Geophysical Union. https://doi.org/10.1029/GM056p0187

Petch, N. J. (1953). The cleavage strength of polycrystals. *Tetsu-To-Hagane/Journal of the Iron and Steel Institute of Japan*, *174*, 25–28.

Phakey, P., Dollinger, G., & Christie, J. (1972). Transmission electron microscopy of experimentally deformed olivine crystals. In H. C. Heard, I. Y. Borg, N. L. Carter, & C. B. Raleigh (Eds.), *Flow and fracture of rocks* (pp. 117–138). Washington, DC: American Geophysical Union.

Pharr, G. M., Herbert, E. G., & Gao, Y. (2010). The indentation size effect: A critical examination of experimental observations and mechanistic interpretations. *Annual Review of Materials Research*, *40*(1), 271–292. https://doi.org/10.1146/annurev-matsci-070909-104456

Poirier, J. P. (1976). On the symmetrical role of cross-slip of screw dislocations and climb of edge dislocations as recovery processes controlling high-temperature creep. *Annales de Readaptation et de Medecine Physique: Revue Scientifique de La Societe Francaise de Reeducation Fonctionnelle de Readaptation et de Medecine Physique*, *11*(6), 731–738.

Proietti, A., Bystricky, M., Guignard, J., Béjina, F., & Crichton, W. (2016). Effect of pressure on the strength of olivine at room temperature. *Physics of the Earth and Planetary Interiors*, *259*(October), 34–44. https://doi.org/10.1016/j.pepi.2016.08.004

Raterron, P., Wu, Y., Weidner, D. J., & Chen, J. (2004). Low-temperature olivine rheology at high pressure. *Physics of the Earth and Planetary Interiors*, *145*(1–4), 149–159. https://doi.org/10.1016/j.pepi.2004.03.007

Renner, J., Evans, B., & Siddiqi, G. (2002). Dislocation creep of calcite. *Journal of Geophysical Research*, *107*(B12), 2364. https://doi.org/10.1029/2001JB001680

Sibson, R. H. (1977). Fault rocks and fault mechanisms. *Journal of the Geological Society*, *133*(3), 191–213. https://doi.org/10.1144/gsjgs.133.3.0191

Sinclair, C. W., Poole, W. J., & Bréchet, Y. (2006). A model for the grain size dependent work hardening of copper. *Scripta Materialia*, *55*(8), 739–742. https://doi.org/10.1016/j.scriptamat.2006.05.018

Singh, A. K., Balasingh, C., Mao, H.-K., Hemley, R. J., & Shu, J. (1998). Analysis of lattice strains measured under nonhydrostatic pressure. *Journal of Applied Physics*, *83*(12), 7567–7575. https://doi.org/10.1063/1.367872

Smith, E., & Worthington, P. J. (1964). The effect of orientation on the grain size dependence of the yield strength of metals. *The Philosophical Magazine: A Journal of Theoretical Experimental and Applied Physics*, *9*(98), 211–216. https://doi.org/10.1080/14786436408229186

Suzuki, I. (1975). Thermal expansion of periclase and olivine, and their anharmonic properties. *Journal of Physics of the Earth*, *23*(2), 145–159. https://doi.org/10.4294/jpe1952.23.145

Thielmann, M., & Kaus, B. J. P. (2012). Shear heating induced lithospheric-scale localization: Does it result in subduction? *Earth and Planetary Science Letters*, *359–360*(December), 1–13.

Thieme, M., Demouchy, S., Mainprice, D., Barou, F., & Cordier, P. (2018). Stress evolution and associated microstructure during transient creep of olivine at 1000–1200°C. *Physics of the Earth and Planetary Interiors*, *278*, 34–46. https://doi.org/10.1016/j.pepi.2018.03.002

Trepmann, C. A., Renner, J., & Druiventak, A. (2013). Experimental deformation and recrystallization of olivine-processes and timescales of damage healing during postseismic relaxation at mantle depths. *Solid Earth*, *4*(2), 423–450. https://doi.org/10.5194/se-4-423-2013

Turcotte, D. L., & Schubert, G. (2014). *Geodynamics*. Cambridge: Cambridge University Press. https://doi.org/10.1017/CBO9780511843877

Underwood, E. E. (1970). *Quantitative stereology*. Reading, MA: Addison-Wesley Pub. Co.

Wallis, D., Hansen, L. N., Ben Britton, T., & Wilkinson, A. J. (2016). Geometrically necessary dislocation densities in olivine obtained using high-angular resolution electron backscatter diffraction. *Ultramicroscopy*, *168*, 34–45. http://www.sciencedirect.com/science/article/pii/S0304399116300821, https://doi.org/10.1016/j.ultramic.2016.06.002

Wang, Y., Durham, W. B., Getting, I. C., & Weidner, D. J. (2003). The deformation-DIA: A new apparatus for high temperature triaxial deformation to pressures up to 15 GPa. *The Review of Scientific Instruments*, *74*(6), 3002–3011. https://doi.org/10.1063/1.1570948

Watts, A. B., & Zhong, S. (2000). Observations of flexure and the rheology of oceanic lithosphere. *Geophysical Journal International*, *142*(3), 855–875. https://doi.org/10.1046/j.1365-246x.2000.00189.x

Weertman, J. (1957). Steady-state creep through dislocation climb. *Journal of Applied Physics*, *28*(3), 362–364. https://doi.org/10.1063/1.1722747

Weertman, J. (1970). The creep strength of the Earth's mantle. *Reviews of Geophysics.*, *8*(1), 145. https://doi.org/10.1029/RG008i001p00145

Weidner, D. J., Vaughan, M. T., Wang, L., Long, H., Li, L., Dixon, N. A., & Durham, W. B. (2010). Precise stress measurements with white synchrotron X rays. *The Review of Scientific Instruments*, *81*(1), 013903. https://doi.org/10.1063/1.3263760

Zhong, S., & Watts, A. B. (2013). Lithospheric deformation induced by loading of the Hawaiian Islands and its implications for mantle rheology. *Journal of Geophysical Research: Solid Earth*, *118*, 6025–6048. https://doi.org/10.1002/2013JB010408

Zhu, T. T., Bushby, A. J., & Dunstan, D. J. (2008). Materials mechanical size effects: A review. *Materials Technology*, *23*(4), 193–209. https://doi.org/10.1179/175355508X376843